An Analysis of Tropical Cyclone Vortex and Convective Characteristics in Relation to Storm Intensity Using a Novel Airborne Doppler Radar Database

MICHAEL S. FISCHER,[a,b] PAUL D. REASOR,[b] ROBERT F. ROGERS,[b] AND JOHN F. GAMACHE[b]

[a] *Cooperative Institute for Marine and Atmospheric Studies, University of Miami, Miami, Florida*
[b] *NOAA/AOML/Hurricane Research Division, Miami, Florida*

(Manuscript received 31 August 2021, in final form 19 May 2022)

ABSTRACT: This analysis introduces a novel airborne Doppler radar database, referred to as the Tropical Cyclone Radar Archive of Doppler Analyses with Re-centering (TC-RADAR). TC-RADAR comprises over 900 analyses from 273 flights into TCs in the North Atlantic, eastern North Pacific, and central North Pacific basins between 1997 and 2020. This database contains abundant sampling across a wide range of TC intensities, which facilitated a comprehensive observational analysis on how the three-dimensional, kinematic TC inner-core structure is related to TC intensity. To examine the storm-relative TC structure, we implemented a novel TC center-finding algorithm. Here, we show that TCs below hurricane intensity tend to have monopolar radial profiles of vorticity and a wide range of vortex tilt magnitudes. As TC intensity increases, vorticity becomes maximized within an annulus inward of the peak wind, the vortex decays more slowly with height, and the vortex tends to be more aligned in the vertical. The TC secondary circulation is also strongly linked to TC intensity, as more intense storms have shallower and stronger lower-tropospheric inflow as well as larger azimuthally averaged ascent. The distribution of vertical velocity is found to vary with TC intensity, height, and radial domain. These results—and the capabilities of TC-RADAR—motivate multiple avenues for future work, which are discussed.

SIGNIFICANCE STATEMENT: Acquiring observations of the inner core of tropical cyclones (TCs) is a challenge due to the hazardous conditions inherent to the storm. A proven method of sampling the TC core region is the use of airborne radar. This study presents a novel database comprising over 900 airborne radar analyses collected in storms between 1997 and 2020, which is freely available to the research community. Here we demonstrate the utility of the database by examining how the three-dimensional structure of the TC core region changes depending upon the intensity of the storm. By identifying how the baseline TC vortex structure varies with TC intensity, this work provides the foundation for multiple future research avenues and model evaluation efforts.

KEYWORDS: Aircraft observations; Convection; Radars/Radar observations; Tropical cyclones

1. Introduction

In recent decades, damage caused by tropical cyclones (TCs) has increased due to an uptick in both coastal population and wealth (e.g., Klotzbach et al. 2018). Destruction caused by TCs is closely related to the intensity of the storm (Klotzbach et al. 2018, 2020). For example, in the United States, it has been estimated that over 80% of all tropical cyclone-related damage is associated with TCs of major hurricane intensity (1-min maximum sustained wind $\geq$ 96 kt; 1 kt $\approx$ 0.51 m s^{-1}) despite the fact that approximately only 20% of all TCs in the North Atlantic basin obtain major hurricane intensity (Pielke and Landsea 1998; Klotzbach et al. 2020). A significant effort has been made to better understand the factors that affect TC intensity, which has contributed to more accurate forecast guidance (DeMaria et al. 2014), as well as a composite improvement in 12–120-h forecast skill of over 8% over the last decade (2010–19) compared to the previous decade (2000–09; Cangialosi et al. 2020). Although some recent progress has been made, TC intensity forecasts continue to struggle with the prediction of events of rapid intensification (RI), which are typically associated with forecast errors over twice as large as non-RI intensity change episodes (e.g., Fischer et al. 2019; Trabing and Bell 2020). Room for improvement exists before operational TC intensity forecasts reach the predictability barrier (Emanuel and Zhang 2016; Cangialosi et al. 2020).

Kinematically, changes in TC intensity are driven by the advection of angular momentum surfaces across the location of maximum wind (e.g., Shapiro and Willoughby 1982; Krishnamurti et al. 2005; Smith et al. 2009; Montgomery and Smith 2014; Smith and Montgomery 2015). In the TC boundary layer, however, where TC intensity is typically defined, angular momentum is not materially conserved, as momentum is lost due to frictional torque and turbulence. Thus, in order to intensify the TC primary circulation within the boundary layer, the inward advection of angular momentum associated with the TC overturning circulation must exceed the rate that angular momentum is lost (Smith and Montgomery 2015). Consequently, heating associated with convective processes within the TC core is vital for maintaining the radial pressure gradient and, thereby, a sufficiently vigorous overturning circulation, required to sustain a given TC intensity.

Consistent with theory, previous observational studies have demonstrated that TC convective organization is closely related to TC intensity. Specifically, TC intensity has been linked to the storm's convective structure, diagnosed by

Corresponding author: Michael S. Fischer, michael.fischer@noaa.gov

DOI: 10.1175/MWR-D-21-0223.1

infrared brightness temperatures (Dvorak 1975; Velden et al. 2006; Ritchie et al. 2012; Fischer et al. 2018), microwave brightness temperatures (Cecil and Zipser 1999; Fischer et al. 2018; Jiang et al. 2019; Wimmers et al. 2019), and estimates of TC precipitation (Chen et al. 2006; Ruan and Wu 2018; Yang et al. 2021). TC convective characteristics have also been shown to be strongly connected to future TC intensity (i.e., intensity change; Guimond et al. 2011; Rogers et al. 2013a; Zagrodnik and Jiang 2014; Kaplan et al. 2015; Alvey et al. 2015; Rogers et al. 2015; Fischer et al. 2018; Wadler et al. 2018). For instance, Fischer et al. (2018) showed that TC intensification occurs preferentially in storms with anomalously symmetric convective structures relative to TCs of similar intensities. Additionally, it was shown that the anomalous convective structure could be used to skillfully predict episodes of RI, which are notoriously challenging periods to accurately forecast. However, the conclusions of the Fischer et al. (2018) analysis were limited by the spatial resolution of the satellite sensors as well as the intermittent temporal coverage of the TC convective cycle inherent to low-Earth orbiting satellites. Furthermore, other studies have pointed out that asymmetric bursts of convection can play important roles in the TC intensity change process, particularly in the intensification process (e.g., Guimond et al. 2010, 2016; Rogers et al. 2016; Hazelton et al. 2017; Wadler et al. 2018). Thus, a more complete understanding of how TC convective structure is related to TC intensity is critical, as knowledge about structural departures from the base state may indicate upcoming changes in TC intensity.

TC intensity change, however, is a multiscale problem. Ultimately, it is the interaction of turbulent- and convective-scale processes with the TC vortex and environment that dictate the intensity evolution of the storm (Rogers et al. 2015; Rios-Berrios et al. 2018; Alvey et al. 2020; Rios-Berrios 2020; Rogers et al. 2020; Chen et al. 2021; Chen and Bryan 2021). Although the environmental conditions favorable for TC intensification are generally well understood, such as low vertical wind shear, high oceanic heat content, and a sufficiently moist troposphere (e.g., DeMaria et al. 2005; Hendricks et al. 2010; Tang and Emanuel 2012; Kaplan et al. 2015; Rios-Berrios and Torn 2017), predicting TC intensification becomes increasingly challenging when a TC is embedded in a marginally favorable environment (Bhatia and Nolan 2013; Zhang and Tao 2013; Rios-Berrios and Torn 2017). For instance, in environments of moderate vertical wind shear, the rate and timing of TC intensification exhibit increased sensitivity to stochastic convective processes, which are intricately connected to the structural evolution of the TC vortex and other nonlinear feedbacks, such as lower-tropospheric ventilation and cold pool development (Zhang and Tao 2013; Rios-Berrios et al. 2018; Rios-Berrios 2020).

The vortex characteristics associated with TC intensity change have also been shown to vary depending on the intensity of the storm. For instance, numerical modeling and observation-based case studies have suggested that in weak TCs (i.e., those of minimal hurricane intensity and below), TC intensification is closely tied to the degree of vertical misalignment of the TC vortex (Rios-Berrios et al. 2018; Chen et al. 2019; Alvey et al. 2020; Rios-Berrios 2020; Rogers et al. 2020; Schecter and Menelaou 2020). However, in an analysis of hurricane-strength TCs, Rogers et al. (2013a) found no significant difference in the magnitude of vortex tilt between intensifying and steady-state TCs. These conflicting findings suggest that it appears possible the significance of vortex misalignment on TC intensity change may also vary depending on TC intensity; however, to the authors' knowledge, no systematic observational study of vortex tilt in relation to TC intensity has yet to be performed.

Moreover, there has been a lack of large-sample-size observational analyses on how the three-dimensional, kinematic TC inner-core structure varies with TC intensity. The hazardous conditions inherent to TCs poses a significant challenge to acquiring in situ observations of TC inner-core structure. Nevertheless, some aspects of the relationship between TC structure and TC intensity have been observed. For instance, McBride (1981) and Frank (1982) used rawinsonde observations to examine the composite kinematic characteristics of TCs stratified by TC intensity; however, the TC inner core could not be properly resolved due to insufficient observations. More recently, the radial variation in TC inner-core structure was assessed in relation to TC intensity via a collection of in situ aircraft reconnaissance observations (Mallen et al. 2005; Martinez et al. 2017); however, because these studies were limited to the flight-level of the aircraft, the vertical variation of the TC inner-core structure could not be analyzed.

The need for a better understanding of how TC convective characteristics and the three-dimensional vortex structure are related to TC intensity serves as the motivation for the present study. Here, we utilize a novel airborne Doppler radar dataset, referred to as the Tropical Cyclone Radar Archive of Doppler Analyses with Re-centering (TC-RADAR). Although airborne Doppler radar observations have been used in multiple previous case studies (e.g., Marks et al. 1992; Reasor et al. 2005; Rogers et al. 2015, 2016; Fischer et al. 2020) as well as composite analyses of mature TCs (e.g., Rogers et al. 2012; Reasor et al. 2013; Rogers et al. 2013a; DeHart et al. 2014; Hazelton et al. 2015; Wadler et al. 2018) to examine TC inner-core structure, these studies did not specifically examine how TC structure varies with intensity. In fact, to our knowledge, no previous studies have used airborne radar observations to assess the composite TC inner-core characteristics for storms below hurricane intensity. Consequently, TC-RADAR provides an unprecedented observational framework to examine TC vortex and convective structure due to the following characteristics of the database:

- A larger sample size and a broader spectrum of TC intensities than those used in previous airborne radar composite analyses, such as Rogers et al. (2012), Reasor et al. (2013), and DeHart et al. (2014).
- The implementation of a novel, objective center-finding algorithm, which is capable of identifying TC centers in the presence of limited data coverage.

TABLE 1. History of NOAA P-3 TDR system characteristics from 1982 to 2021. Processing using pulse compression and time frequency modulated (TFM) pulses are indicated by the † and * symbols, respectively. The number in parentheses indicates the number of radars of the specified type. RVP is a trademark of SIGMET/Vaisala. CRPE and NSSL are used as abbreviations for the Centre de Recherches en Physique de L'Environnement Terrestre et Planetaire and the National Severe Storms Laboratory, respectively.

Years	Transmitter(s)	Antenna(s)	Signal processor
1982–87	Magnetron	NOAA-built parabolic (1)	NSSL-built
1988–90	Magnetron	NOAA-built parabolic (2)	RVP-5
1991–2011	Magnetron	NOAA-built parabolic (1) and CRPE-built flat plate (1)	RVP-5
2012–15	Magnetron	CRPE-built flat plate (1) and Malibu-built flat plate (1)	RVP-8
2016	Magnetron	Malibu-built flat plate (2)	RVP-900
2017/18	Dual solid state	Malibu-built flat plate (2)	RVP-900†
2019–21	Dual solid state	Malibu-built flat plate (2)	RVP-900†,*

- The inclusion of metadata pertaining to the vortex intensity, location, and environmental conditions.
- The database is publicly available in a more user-friendly format than previous airborne radar datasets.

Thus, the goals of this study are twofold: 1) to demonstrate the utility of TC-RADAR to the research community and 2) to use TC-RADAR to gain a better understanding of how TC vortex and convective characteristics are related to TC intensity.

2. Data and methods

a. Radar processing

This study utilizes observations from NOAA's WP-3D (P-3) tail Doppler radar (TDR). The TDR is a 360° vertically scanning X-band (3.22 cm) radar. The TDRs on the two NOAA P-3s have undergone a series of changes in antenna, signal processor, and transmitter since their installation in the 1980s, as summarized in Table 1. While these changes have necessitated frequent adaptations of the radar data quality control process, the resulting reflectivity and Doppler velocity datasets are similar in their basic characteristics. One exception is the most recent upgrade to a dual-transmitting solid state system in 2017, with its greater sensitivity (due to pulse compression) and increased frequency of observation along the flight track. The increased sensitivity—approximately 15 dB—has permitted greater coverage in the 12–16-km layer, documenting the TC outflow layer much better than before.

For all analyses considered here, the fore-aft scanning technique (FAST; Jorgensen and DuGranrut 1991; Jorgensen et al. 1996) was employed in which the antenna scans fore and aft of the fuselage in an approximately 20° cone relative to a vertical plane. FAST allows for the retrieval of three-dimensional winds, where sufficient scatterers exist, as the aircraft passes through the TC (Gamache et al. 1995; Lorsolo et al. 2010). Doppler velocity and reflectivity measurements collected during an observation period first undergo an automated quality control process (Gamache 2005) and are then interpolated onto a Cartesian grid in a manner similar to Eq. (2) of (Gao et al. 1999), with a horizontal grid spacing of 2 km × 2 km and a vertical grid spacing of 0.5 km. Finally, the three-dimensional wind is retrieved using a variational technique which simultaneously solves the radar projection equations and mass continuity equation subject to boundary conditions and a second-derivative filter (Gamache 1997; Gao et al. 1999; Reasor et al. 2009). Because of the grid spacing of the analysis and the Gaussian filtering being employed, features with wavelengths less than 12 km in the horizontal and 3 km in the vertical may be insufficiently resolved. Some of the sources of error in the TDR analyses, such as those arising from incomplete sampling, boundary conditions, second-derivative filtering, and the discretized solution of the mass-continuity equation were quantified by Lorsolo et al. (2013); however, other sources of error exist. A more comprehensive quantification of TDR analysis errors is the subject of ongoing work.

TDR analyses use observations from both the inbound and outbound flight legs from the TC center, collectively referred to as a center pass, and, in some cases, also include either the upwind or downwind leg tangential to the TC center. A typical radial leg length is 105 n mi (~195 km), although it can be somewhat shorter depending on the mission. Radial legs rarely exceed this scale. Thus, the maximum total length of a center pass is approximately 400 km. For a given TC center pass, the mapped radar analyses provide a glimpse of the three-dimensional TC kinematic structure within a corridor near the flight track. A representative example of these so-called swath observations is shown in Fig. 1a. In typical operating conditions, the maximum unambiguous radial range is approximately 50 km, which is reflected by the edge of TDR observations seen in Fig. 1a. At some locations, the radial extent of observations is even smaller due to either attenuation, variations in beam geometry as the aircraft maneuvers, a lack of sufficient scatterers, removal of data such as surface clutter from the automated quality control process, or some combination of these factors. The issue of limited coverage associated with individual swath analyses can be remedied if the reconnaissance flight makes multiple passes through the center of the TC at varying azimuthal headings. For such flights, the increase in azimuthal coverage of data is leveraged through "merged" analyses, which are storm-centered composites that average all swath data for a given flight (Fig. 1b). With the assumption that the TC vortex does not significantly evolve during the typical 3–6-h sampling

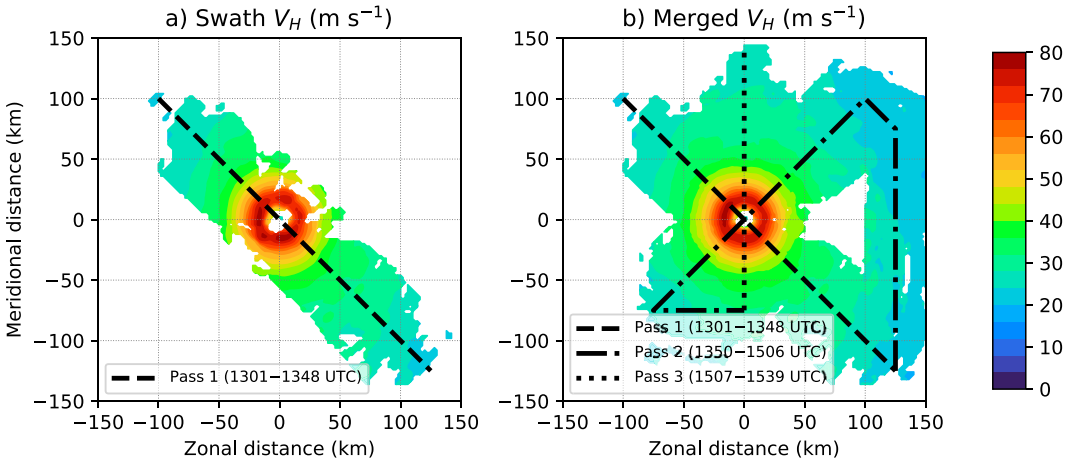

FIG. 1. (a) Storm-centered, motion-relative, TDR-derived horizontal wind speed (shaded; m s^{-1}) at a height of 2 km obtained from the 1324 UTC 1 Sep center pass into Hurricane Dorian (2019) as part of the 20190901H1 mission. The approximate flight track is shown by the black-dashed line, with the duration of the observing period shown in the legend. This pass serves as a representative example of swath data. (b) As in (a), but for the corresponding merged analysis using swath data from all three center passes in the 20190901H1 mission. The corresponding flight track for each TDR swath analysis is shown by a unique dash style, as denoted in the legend.

period of a single flight, merged analyses provide a more robust visualization of the TC vortex structure at the expense of smoothing transient features in the TC circulation. Merged TDR analyses have been successfully used by multiple previous studies to examine TC inner-core structure (e.g., Rogers et al. 2012; Reasor et al. 2013; Rogers et al. 2013a; Hazelton et al. 2015).

In the course of examining the flow characteristics of TCs across the entire database, a change in synthesis method was discovered which must be addressed. The majority of analyses for years prior to 2010 in TC-RADAR were created with a version of the processing software having too much second-derivative filtering in the vertical direction in an initial low-azimuthal wavenumber analysis of the data. This initial analysis, which is used as a low-weight background field in the variational method, permitted vertical motions that were both too deep and strong in the final analysis. The low-weight background addresses the unbounded nature of the continuity solution near the aircraft track (Chong and Testud 1996). Exacerbating this issue was the extension of the initial low-wavenumber analysis far beyond the grid points constrained by Doppler data. Occasionally, extreme values of vertical wind can be identified in regions of reflectivity that are relatively isolated and lacking any vertical structure typical of convection, highlighting their nonphysical origin. On rare occasions, these poor background fields might also have affected the de-aliasing and QC (which are aided by the background wind field) of the final Doppler interpolation. All TDR analyses from 2010 to the present were generated with proper second-derivative filtering of the background field and with the initial low-wavenumber analysis limited to regions constrained by Doppler data. In addition to yielding more physically reasonable retrievals of vertical motion, these changes also greatly reduced occurrences of spurious vertical motion. The only other changes made since 2010 were efforts over time to improve quality control and de-aliasing, to adapt to changes in the technology, and differences between flights in the noisiness of the data. Because the impact of the aforementioned issues on the horizontal winds was deemed relatively minor, all cases within TC-RADAR are included in section 3, which focuses on the horizontal component of the flow. The inclusion of all TC TDR analyses in section 3 enhanced the total sample size and increased confidence in the presented results. In section 4, where the focus shifts to the TC secondary circulation and convective structure, only cases since 2010 are included to avoid the introduction of biases associated with the change in solution method into our results.

b. *Distribution of cases in TC-RADAR*

TC-RADAR is a collection of radar analyses from 273 flights into 63 unique TCs and 3 different pre-TC disturbances in the North Atlantic, eastern North Pacific, and central North Pacific basins between 1997 and 2020 (Fig. 2). TC-RADAR contains storms ranging from pre-genesis disturbances to mature hurricanes, which builds upon the cases used in previous composite studies, such as Rogers et al. (2012), Reasor et al. (2013), Rogers et al. (2013a), and Wadler et al. (2018). To our knowledge, TC-RADAR is the largest radar-based observational dataset of TC structure to be introduced in the literature.

A unique aspect of TC-RADAR is the inclusion of best track and environmental metadata from the Statistical Hurricane Intensity Prediction Scheme (SHIPS; DeMaria and Kaplan 1994; DeMaria et al. 2005) diagnostic files for each TDR analysis. For swath analyses, the synoptic time nearest to the TC center fix is used to obtain the relevant

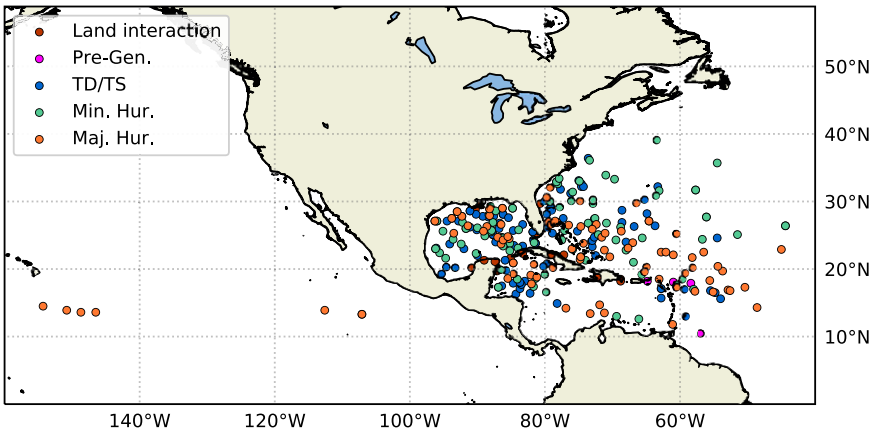

FIG. 2. Geographic locations for all TDR analyses included in the TC-RADAR database. TC locations are identified using the best track entry associated with the nearest synoptic time to the midpoint of the observing period. TDR analyses for TCs of tropical depression and tropical storm intensity are depicted by the blue circles. Analyses for TCs of minor hurricane intensity and major hurricane intensity are depicted by the green and orange circles, respectively. The locations of pre-genesis disturbances are depicted by the center of the TDR analysis domain for each case (pink circles). TDR analyses for TCs located within 50 km of land (as identified from the SHIPS "DTL" parameter) are shown by the red circles. Neither pre-genesis disturbances nor land interaction cases are utilized in this study.

best track and environmental metadata. For merged analyses, the synoptic time nearest to the midpoint of the first and last center fixes of the flight are used to obtain the relevant metadata. Although the nearest synoptic time and the time of the TDR analysis can differ by up to three hours, the best track and environmental metadata are assumed to be representative of the conditions associated with the TC at the time it was observed by the aircraft.

For the purposes of this study, we only used analyses from TCs of at least tropical depression intensity and those that were at least 50 km away from a major landmass[1] at the time of nearest best track analysis with the aim of removing TC structural influences associated with land interaction. Imposing these criteria left 249 merged analyses, including TCs spanning a wide range of intensities (Figs. 3a,b). The distribution of TC intensities in TC-RADAR exhibits a bimodal distribution with a first peak between 50 and 60 kt and another peak between 100 and 120 kt (Fig. 3a). The translation speed of the storms in TC-RADAR nearly exclusively ranges from 0 to 10 m s^{-1}. Environmental diagnostics from SHIPS reveal the TCs analyzed in this study exist in environments associated with a wide range of deep-layer (850–200 hPa) shear magnitudes[2] (Fig. 3d) and midlevel (700–500 hPa) moisture (Fig. 3e). All of the TCs analyzed here occurred over sea surface temperatures (SSTs) $>$ 26°C, with the majority over SSTs $\geq$ 29°C.

[1] Determined using the SHIPS distance to land (DTL) parameter.

[2] Determined using the SHIPS SHDC parameter. This metric uses a vortex removal process and computes the mean shear within 0–500 km from the TC center. Hereafter, all references to shear will use this metric.

c. *TC center identification*

To assess the vortex and convective characteristics of each TC, a TC center must be identified that is consistent with the time of the TDR analysis. Determining the center of a TC is not a trivial task (Nguyen et al. 2014; Ryglicki and Hodyss 2016; Ryglicki et al. 2021), especially using an observational platform that does not contain analyses of the TC mass field and often has large gaps in data coverage, such as the TDR. Although objective methods of identifying TC centers via TDR observations have been used in previous studies (e.g., Reasor and Eastin 2012; Rogers et al. 2012; Reasor et al. 2013), these studies employed methods tailored to the analysis of storms of hurricane intensity. To summarize, the aforementioned studies identified the TC center as the location that yields the maximum azimuthally averaged tangential wind within a set of annuli of varying widths, centered on the TC's radius of maximum wind. When we attempted to replicate this method in TCs weaker than hurricane intensity, we found that these weak TCs can be associated with ill-defined and asymmetric regions of peak wind as well as larger observational gaps due to a dearth of scatterers, which occasionally resulted in center estimates that substantially differed from subjective TC center estimates based on either vorticity maxima or storm-relative circulation centers.

The novel TC center-finding technique used in this study is described in detail in the appendix. In essence, the TC center is objectively identified as the TDR analysis grid point where the storm-relative flow best matches an idealized vortex of purely cyclonic flow. The novel method was found to routinely identify a TC center that is located within a region of enhanced vorticity and close to the circulation center of the storm-relative flow. By employing the novel center-finding

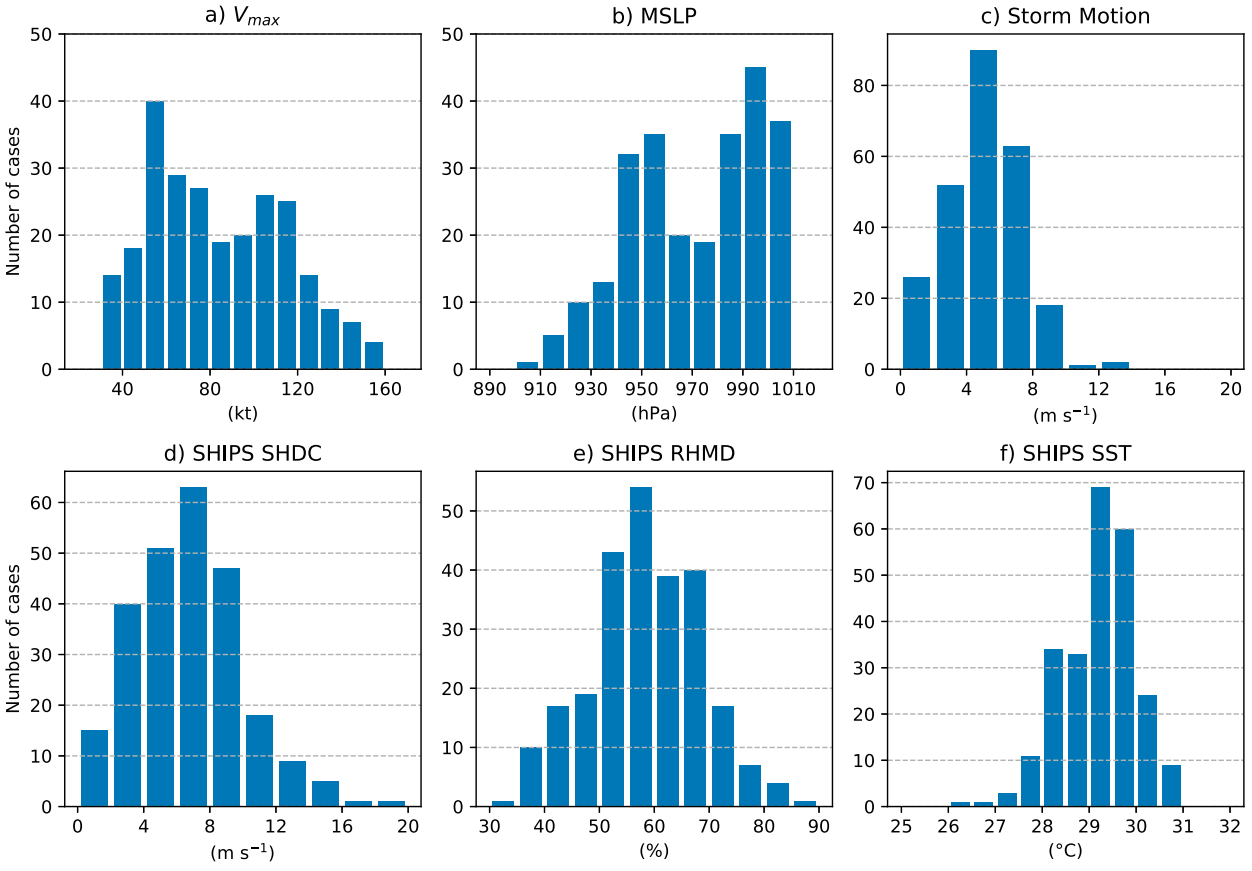

FIG. 3. (a) Histogram of best track intensity (V_{max}; kt) for all TCs in TC-RADAR at least 50 km away from land. (b),(c) As in (a), but for the minimum central pressure (hPa) and the storm translation speed (m s^{-1}), respectively. (d)–(f) As in (a), but for the 850–200-hPa vertical wind shear magnitude (SHDC; m s^{-1}), the 700–500-hPa layer-averaged relative humidity (RHMD; %), and the sea surface temperature (SST; °C), respectively, derived from SHIPS analyses. In each panel, the bottom bound of the histogram bin is inclusive, while the upper bound is not inclusive.

technique, this study was able to examine storm-centered airborne radar composites of TCs below hurricane intensity for what we believe to be the first time.

d. Computing vortex tilt

With confidence in the novel center-finding technique, all swath analyses were re-centered using the motion-relative horizontal wind at a height of 2 km. In TC-RADAR, the re-centered, gridded observations are stored within a storm-centered domain that spans 300 km × 300 km. Merged analyses were then generated using the re-centered swaths available for each flight. Using the merged analyses, objective TC center estimates were computed at all vertical levels below 14 km, provided the maximum azimuthally averaged tangential wind relative to the diagnosed center location at the current height was at least 8 m s^{-1}. This threshold ensured a sufficiently robust vortex was being re-centered. Following the identification of all TC centers, vortex tilt is computed for each TC, relative to a base center at a height of 2 km. This study only uses vortex tilt derived from merged analyses, due to the greater azimuthal data coverage and more confident TC center estimates compared to those derived from TDR swath analyses.

Examples of two tilted storms are shown in Fig. 4 for flights into Tropical Storm Jerry (2019) and Isaias (2020). The horizontal plan-views of the storm-relative horizontal wind field in Tropical Storm Jerry, shown here in 2-km vertical increments, reveal an eastward tilt with height relative to the 2-km vortex center (Figs. 4b,c). A more prominent example of vortex misalignment was observed in Isaias (Figs. 4d–f). Although observational coverage was confined to the northeastern portion of the vortex, the 6-km TC center identified in the analysis was displaced approximately 100 km to the east-northeast of the 2-km TC center (Fig. 4f).

Hodographs of vortex tilt for the same TDR analyses of Jerry and Isaias more clearly illustrate the vertical structure of their vortex misalignment (Fig. 5). In Jerry, the vertical profile of tilt increases rather consistently with height (Fig. 5a); however, in Isaias, a sharp jump in tilt magnitude is observed between 4 and 4.5 km, suggesting a decoupling of the low-level and midlevel vortex (Fig. 5b). Although a wide range of vortex misalignment configurations exist in nature, these results

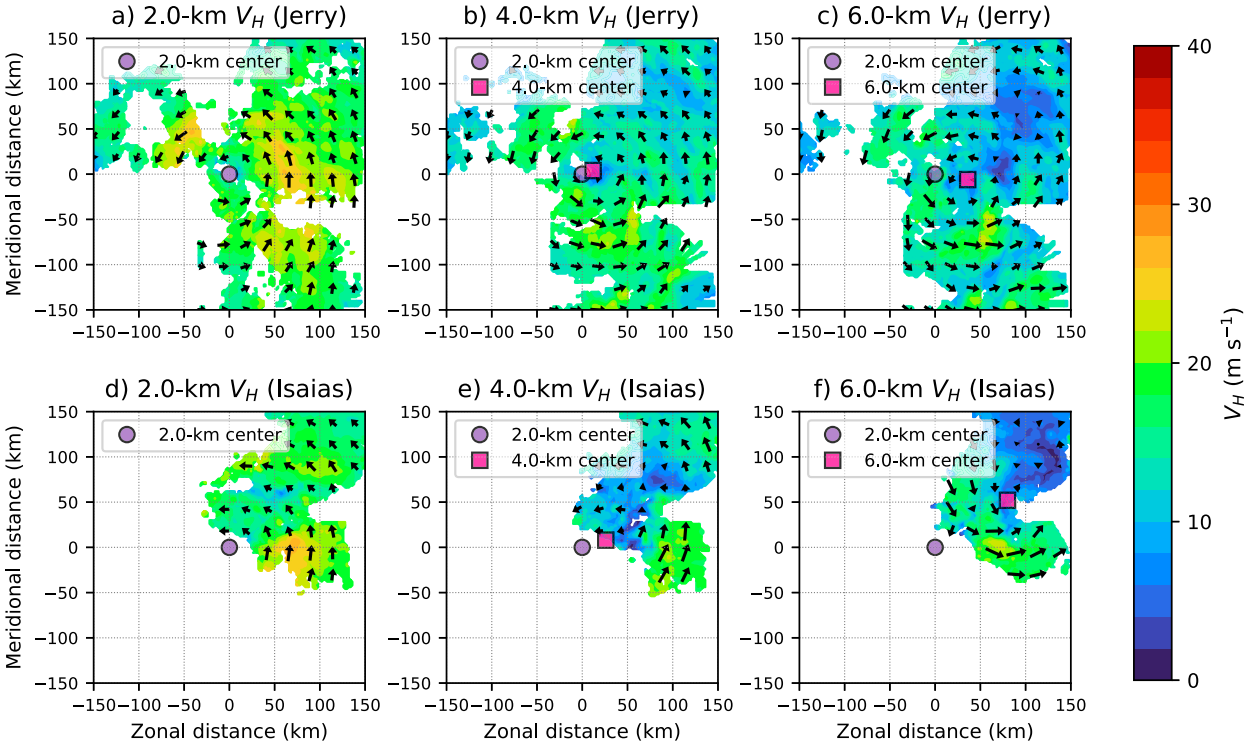

FIG. 4. (a) Storm-centered, motion-relative, TDR-derived merged analyses of horizontal wind speed (shaded; V_H; m s^{-1}) at a height of 2 km for the 190922H1 mission into Tropical Storm Jerry. The midpoint time for the creation of the analysis was 1749 UTC 22 Sep 2019. The corresponding wind direction is shown in the black vectors. The 2-km TC center is denoted by the purple dot. (b),(c) As in (a), but at a height of 4 and 6 km, respectively. The tilt-relative TC center at each height is denoted by the pink square. (d)–(f) As in (a)–(c), but for the 200801I2 mission into Tropical Storm Isaias (2020). The midpoint time for the creation of the analysis was 0036 UTC 2 Aug 2020.

demonstrate the utility of the novel center-finding method to diagnose the degree of misalignment.

3. The relationship between TC intensity and vortex structure

a. TC intensity versus inner-core size

With a center-finding algorithm established, the relationship between TC intensity and TC kinematic structure was explored. Figure 6a shows the distribution of TDR-derived TC radius of maximum wind (RMW), at a height of 2 km, as a function of TC intensity. Due to the limited domain size arising from typical observational coverage, the largest radial range we were able to consistently search for an RMW was 150 km. Consequently, it is possible the few storms analyzed here with an RMW of 150 km had slightly larger RMWs in reality. Nevertheless, Fig. 6a shows TCs below hurricane intensity (i.e., those with maximum sustained 10-m winds < 64 kt) are associated with a wide range of RMWs, while major hurricanes (maximum sustained 10-m winds ≥ 100 kt) are generally associated with RMWs ≤ 80 km. The link between more intense TCs and smaller RMWs is consistent with previous studies (Knaff et al. 2015; Martinez et al. 2017).

The size of the RMW for a given TC intensity has implications for the pressure–wind relationship of the TC (Fig. 6b). Storms with relatively large RMWs for a certain maximum-sustained wind speed tend to have lower central pressures than storms with relatively small RMWs for the same maximum-sustained wind speed. These findings are consistent with previous analyses of influences on the TC pressure–wind relationship (Knaff and Zehr 2007; Kossin 2015).

The relationship between the best track intensity and the maximum Earth-relative, TDR-derived wind speed at a height of 2.0 km is shown in Fig. 6c. There is a strong correlation between the maximum radar-derived wind speed and the best track intensity, indicating the accuracy of the best track intensity estimates. The high bias in TDR-derived wind is primarily related to the differences in height of the wind observations compared to the 10-m maximum wind in the best track, but differences may also arise because the best track estimates peak wind based on a synthesis of available spaceborne, airborne, ground radar, and in situ observing platforms. Nonetheless, the bulk of the TDR-derived maximum winds are approximately 10%–15% larger than the best track maximum 10-m winds, consistent with the wind-reduction factors found by Franklin et al. (2003). There are some instances where the maximum TDR-derived winds are less than the best track intensity estimates; however, in a majority of these cases, the RMW of the TC was less than 50 km. It is possible that for these relatively compact inner cores, the wind maxima were not entirely resolved by the TDR analyses.

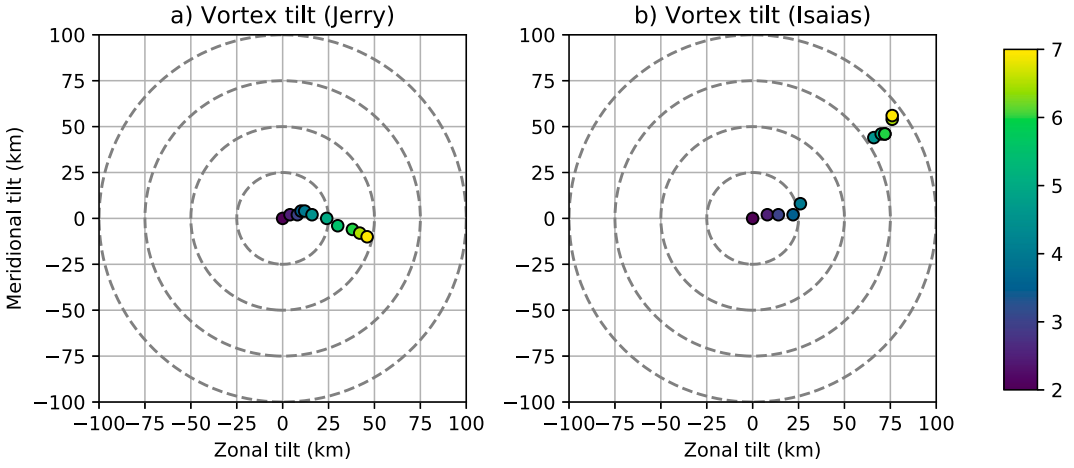

FIG. 5. (a) Vertical profile of vortex tilt for the 190922H1 mission into Tropical Storm Jerry. Observations are taken from the same analysis shown in Figs. 4a–c. Here, tilt is computed relative to the TC center at a height of 2 km and shown in 0.5-km increments in the vertical. The color of the circles corresponds to the height of the center estimate. (b) As in (a), but for the 200801I2 mission into Tropical Storm Isaias, corresponding to Figs. 4d–f.

Additionally, it is likely neither the TDR analyses nor the best track capture the true maximum wind within a TC, as observations and large-eddy simulations have suggested peak winds in the TC boundary layer occur within turbulent eddies, which are unlikely to be reflected in either intensity estimate (e.g., Marks et al. 2008; Guimond et al. 2018; Stern and Bryan 2018).

b. *Azimuthally averaged vortex characteristics*

Composites of azimuthally averaged, TDR-derived quantities were constructed using a normalized radial coordinate system, similar to previous studies such as Rogers et al. (2012). Here, the radial coordinate R^* is scaled by the RMW at a height of 2 km for each TC, such that a value of $R^* = 1$ denotes the location of the TC's RMW. This normalization process better accounts for variations in TC size and yields more insightful composites. All composites using the normalized radial coordinate system were constructed from TDR merged analyses that had data coverage $\geq 50\%$ in the azimuthal direction at the corresponding location in radius–height space.

To assess how the structure of the TC primary circulation is related to TC intensity, Fig. 7 shows composites of azimuthally averaged relative vorticity ($\overline{\zeta}$) and tangential wind ($\overline{V_T}$) for three TC intensity groups. Here, ζ was computed on a Cartesian grid prior to the calculation of the azimuthally averaged values shown in Fig. 7. The intensity group definitions and the number of corresponding TDR analyses are shown in Table 2.

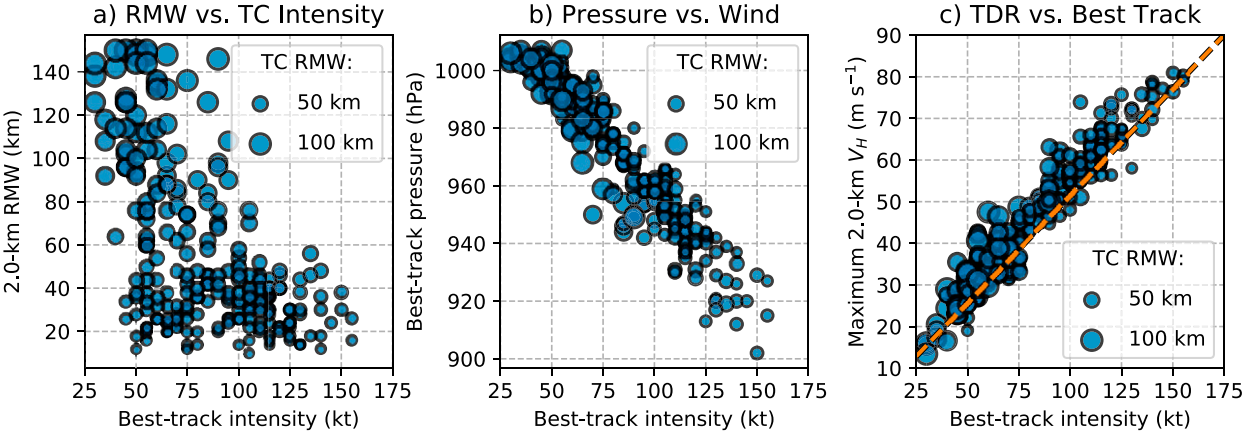

FIG. 6. (a) Scatterplot of maximum sustained 10-m Earth-relative wind speed (kt), derived from best track data, vs the radius of maximum wind (RMW) at a height of 2 km, determined from the azimuthally averaged tangential wind. The size of each data point is proportional to the TC RMW, with select sizes shown in the figure legend. (b) As in (a), but the relationship between best track maximum sustained 10-m winds (kt) and minimum central pressure (hPa). (c) As in (a), but for the relationship between maximum sustained 10-m wind speed (kt) according to best track, vs the maximum TDR-derived wind speed (m s^{-1}) from merged analyses at a height of 2 km. The orange, dashed line depicts the one-to-one relationship.

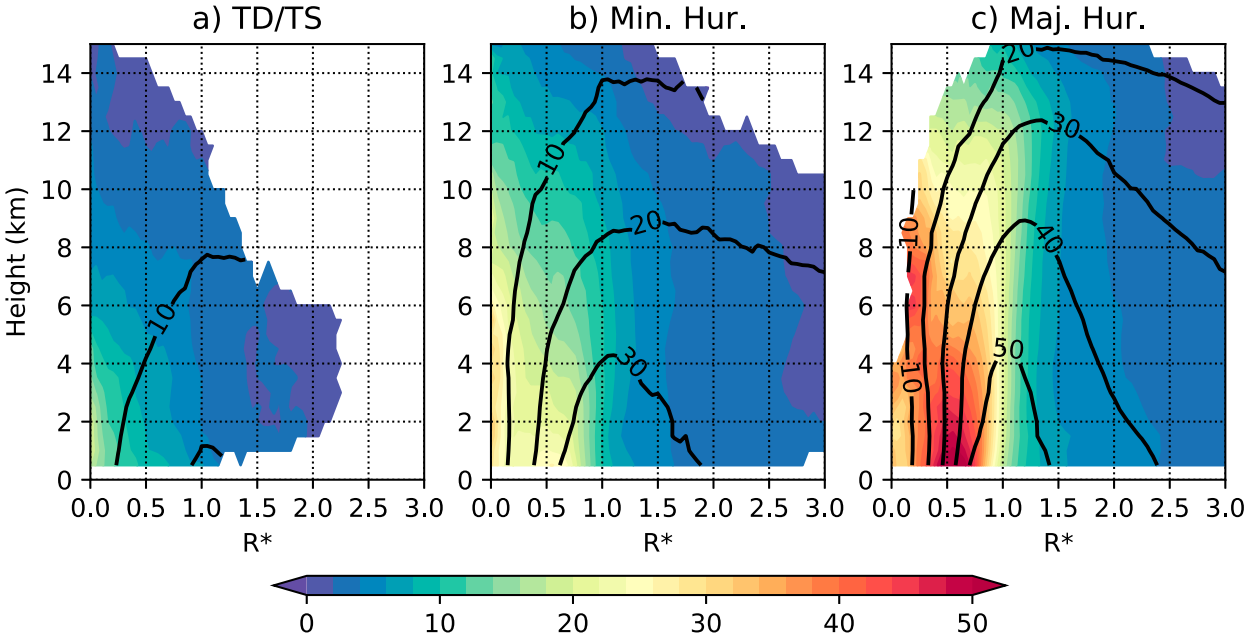

FIG. 7. (a) Composite-mean, azimuthally averaged relative vorticity ($\overline{\zeta}$; shaded; 10^{-4} s^{-1}) for TCs of tropical depression and tropical storm intensity. Values are shown with respect to height (km) above sea level and normalized radius (R^*), where $R^* = 1$ is the radius of maximum wind at a height of 2 km. Azimuthally averaged tangential wind ($\overline{V_T}$) is contoured in black every 10 m s^{-1}. Composite values are only plotted for grid points where at least 20 merged analyses had observations. (b),(c) As in (a), but for TCs of minor hurricane and major hurricane intensity, respectively.

The composites of $\overline{\zeta}$ reveal differences in the radial structure of the TC vortex (Fig. 7). TCs below hurricane intensity tend to have monopolar vorticity profiles over a deep layer (Fig. 7a). The composite of $\overline{\zeta}$ for minor hurricanes displays two maxima in vorticity (Fig. 7b). The first $\overline{\zeta}$ maximum is consistent with a monopolar vortex structure, while the second maximum is found along the inner edge of the RMW. The inner $\overline{\zeta}$ maximum is more pronounced than the outer $\overline{\zeta}$ maximum, especially in the midtroposphere between 4 and 8 km. TCs of major hurricane intensity tend to be associated with ring-like vorticity maxima centered near $R^* = 0.5$ below 4 km, with signs of a secondary, inner maximum in $\overline{\zeta}$ above 4 km (Fig. 7c). Subjective inspection of the individual merged analyses that comprise the major hurricane composite revealed the inner, secondary maximum in $\overline{\zeta}$ in major hurricanes is typically the result of decaying relict eyewalls following an eyewall replacement cycle (e.g., Sitkowski et al. 2012). In a few other cases, the inner, secondary maximum in $\overline{\zeta}$ appeared to be the result of inward vorticity mixing from the TC eyewall (e.g., Schubert et al. 1999; Kossin and Schubert 2001). Despite this subset of cases, a lower-tropospheric vorticity ring was consistently seen in the subjective analysis of major hurricanes.

The bimodal structure of lower-tropospheric $\overline{\zeta}$ in minor hurricanes (Fig. 7b) resembles composites of flight-level reconnaissance observations examined by Martinez et al. (2017), who showed intensifying minor hurricanes feature ring-like radial vorticity profiles, whereas steady-state and weakening minor hurricanes have monopolar vorticity structures. Although the present study has not investigated how the radial vorticity profile is related to TC intensity change, from the results shown in Fig. 7, it appears plausible that a ring-like vorticity profile in the lower troposphere is a configuration that supports major hurricanes and TCs soon to become major hurricanes.

In addition to the intensity-dependent differences in the radial structure of the TC vortex, TC intensity was also linked to differences in the vertical decay of the TC vortex (Fig. 8). To account for the inherent disparities in the magnitudes of the azimuthally averaged tangential wind ($\overline{V_T}$) field for each TC intensity group, Fig. 8 shows vertical profiles of the

TABLE 2. Best track intensity (V_{max}) bounds and the number of TDR swath and merged analyses for the three TC intensity groups where sufficient data coverage was present to examine TC vortex characteristics (using all years in TC-RADAR).

TC intensity group	Intensity range (kt)	No. of swath analyses	No. of merged analyses
TD/TS	$V_{max} < 64$	233	74
Minor hurricane	$64 \le V_{max} < 96$	260	79
Major hurricane	$V_{max} \ge 96$	287	84

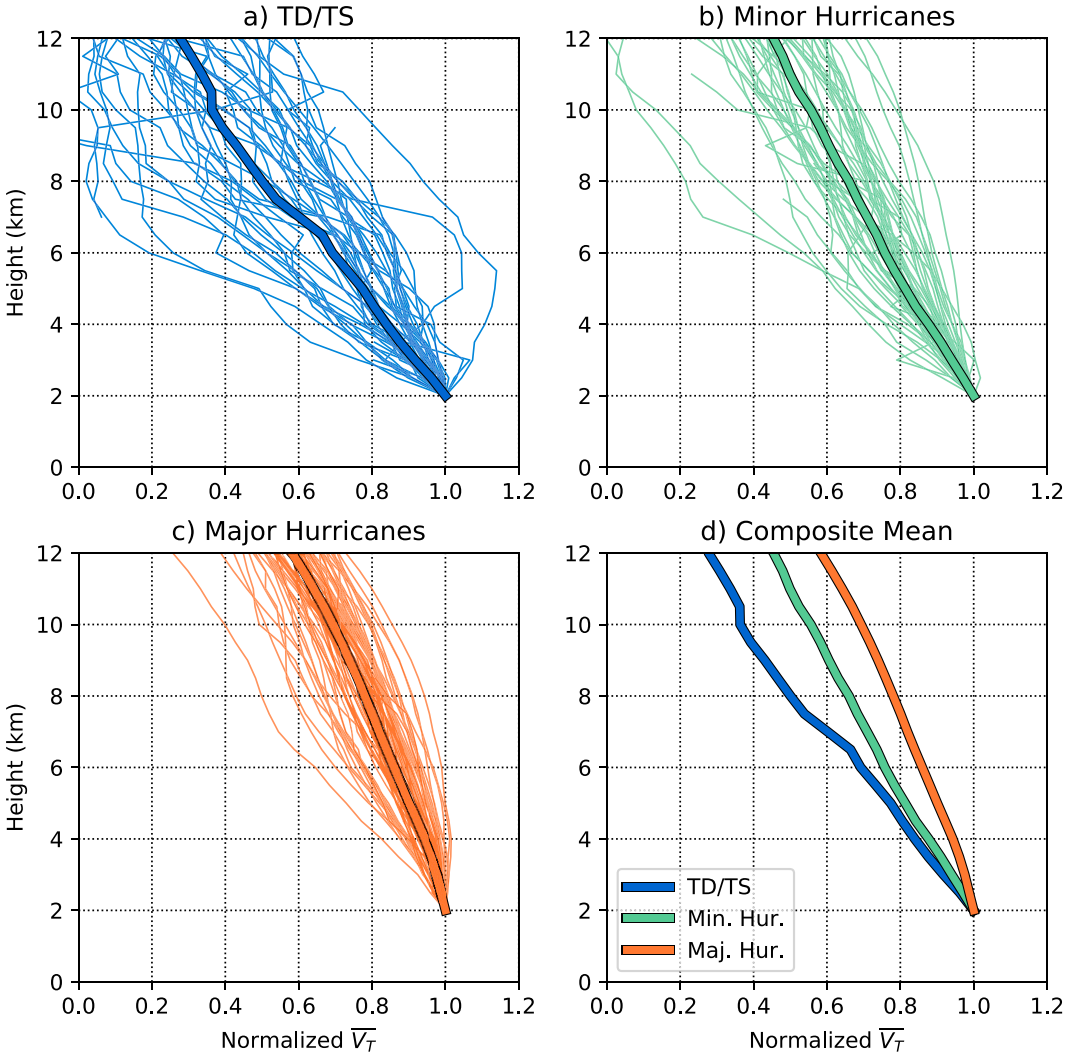

FIG. 8. (a) Vertical profiles of normalized $\overline{V_T}$ (relative to the value at a height of 2.0 km) for all TCs of tropical depression and tropical storm intensity. The composite-mean profile is shown by the thicker line. Normalized $\overline{V_T}$ is computed relative to the TC position at a height of 2 km. (b),(c) As in (a), but for TCs of minor hurricane intensity, and major hurricane intensity, respectively. (d) As in (a)–(c), but for solely the composite-mean profiles of each TC intensity group.

maximum value of $\overline{V_T}$ at each altitude for each merged analysis, normalized by the maximum value of $\overline{V_T}$ at a height of 2.0 km. This normalization process is similar to that done by Stern and Nolan (2011) and Stern et al. (2014) who also examined the vertical decay of the $\overline{V_T}$ field using TDR observations for a smaller number of storms of hurricane intensity.

In corroboration with the findings of Stern et al. (2014), it was found that more intense TCs are characterized by more gradually decaying vertical profiles of normalized $\overline{V_T}$. For example, in storms below hurricane intensity, the mean value of normalized $\overline{V_T}$ at a height of 8 km is approximately 50% of that at a height of 2 km, whereas for minor and major hurricanes, this value is 66% and 78%, respectively, of the mean, normalized $\overline{V_T}$ at 2 km. However, there is considerable spread in normalized $\overline{V_T}$ at a height of 8 km for TCs below hurricane intensity, suggesting relatively weak TCs are associated with large variability in vortex depth (Fig. 8a). The differences in vortex depth in relation to TC intensity imply differences in the relevant steering layers for the track of each storm (Velden and Leslie 1991; Galarneau and Davis 2013; Hazelton et al. 2018). Thus, this analysis indicates that errors in TC intensity forecasts may impact TC track forecasts for those storms embedded in a vertically sheared environmental flow.

c. *TC intensity versus vortex tilt*

Multiple previous studies have demonstrated how vertical wind shear can act to tilt the TC vortex from an otherwise upright position (e.g., Jones 1995; Wang and Holland 1996; Reasor et al. 2004, 2013; Reasor and Montgomery 2015;

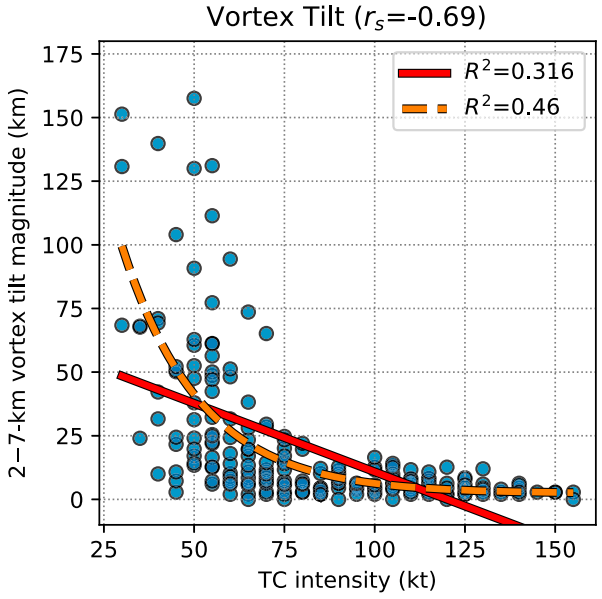

FIG. 9. Scatterplot of the 2–7-km vortex tilt magnitude (km), as a function of best track TC intensity (kt). Each point represents a unique analysis. A linear fit to the distribution is shown by the red, solid line, and an exponentially decaying fit is shown by the dashed, orange line. The square of the correlation coefficients (R^2) is shown in the legend. The rank correlation coefficient is denoted by r_s.

Rios-Berrios et al. 2018). The eventual alignment of a tilted TC vortex has been hypothesized to be critical for TC intensification, especially in TCs below hurricane intensity (e.g., Chen et al. 2018a; Rios-Berrios et al. 2018; Alvey et al. 2020; Rogers et al. 2020; Schecter and Menelaou 2020). However, in an observational analysis of TCs of hurricane intensity, Rogers et al. (2013a) did not find significant differences in the vortex tilt of intensifying and steady-state TCs, with most TCs associated with generally upright vortices. This raises the question of whether vortex tilt displays a dependency on TC intensity.

Figure 9 shows the distribution of the 2–7-km vortex tilt magnitude as a function of TC intensity for all merged analyses where a TC center estimate at a height of 7 km could be made. A statistically significant relationship exists between TC intensity and vortex tilt magnitude, with a rank correlation coefficient of −0.69. This relationship exhibits nonlinear characteristics, as an exponentially decaying fit yielded a larger squared correlation coefficient (0.46) than that of a linear fit (0.316). This nonlinear relationship is particularly evident for TCs below hurricane intensity, where a large range of tilt magnitudes are observed, with some TCs exhibiting a 7-km center displacement in excess of 100 km. Alternatively, major hurricanes were consistently associated with more upright vortices, as tilt magnitudes never exceed 25 km. Although this relationship appears consistent with modeling simulations (e.g., Zhang and Tao 2013; Chen et al. 2018b; Ryglicki et al. 2018; Rios-Berrios 2020; Schecter and Menelaou 2020) and previous case studies (e.g., Reasor and Eastin 2012; Stevenson et al. 2014; Nguyen et al. 2017; Rogers et al. 2020; Boehm and Bell 2021; Ryglicki et al. 2021; Alvey et al. 2022), it is our understanding that this is the first time the link between vortex tilt magnitude and TC intensity has been quantified using an observational dataset of this scale.

To better illustrate the tilt profile for each available merged analysis, Fig. 10 shows shear-relative hodographs of vortex tilt for the same three TC intensity groups analyzed earlier. In each intensity group, the majority of TCs exhibit a tilt direction that is downshear-left of the 2-km TC center location, which is consistent with previous theoretical and observational studies (e.g., Wang and Holland 1996; Reasor et al. 2004, 2013). Weak TCs display the largest spread in both tilt magnitude and shear-relative tilt direction of the three intensity groups (Fig. 10a). The composite-mean tilt profiles for each intensity group are associated with similar shear-relative directions (Fig. 10d); however, significant differences exist in the mean magnitudes of vortex tilt for each intensity group. TCs below hurricane intensity have a mean 2–7-km tilt magnitude of approximately 46 km, while minor hurricanes and major hurricanes have mean tilt magnitudes of 11 and 6 km, respectively. Differences in tilt magnitude for each intensity group were found to be statistically significant at the 99.9% confidence level using the nonparametric, two-tailed Wilcoxon rank sum test (Wilks 2011). These results demonstrate that TC intensity is strongly related to vortex tilt characteristics.

4. The relationship between TC intensity and convective structure

a. Azimuthally averaged convective characteristics

TC intensity is fundamentally connected to the balance between the import of angular momentum in the TC boundary layer and the loss of angular momentum via friction (Smith et al. 2009). Heating associated with convective processes in the TC inner core is vital toward maintaining an inward-directed pressure gradient force, which may advect angular momentum surfaces inward. In accordance, previous studies have demonstrated a relationship between TC intensity and TC convective structure, as identified via satellite observations from geostationary and passive microwave satellite imagery (e.g., Dvorak 1975; Cecil and Zipser 1999; Velden et al. 2006; Fischer et al. 2018). However, the signal between TC intensity and the kinematic characteristics of the TC secondary circulation has yet to be systematically evaluated in an observational framework for all TC intensities.

To begin to address this gap, Fig. 11 shows the composite radial wind and vertical velocity (i.e., the secondary circulation) for the three intensity groups. As discussed in section 2a, the analyses of TC convective structure in this section only consider TCs that occurred between 2010 and 2020, as these TCs were associated with a consistent version of the synthesis software. Although this temporal constraint causes a reduction in sample size, particularly for TCs of hurricane intensity (Table 3), it ensures a more homogeneous comparison of TC vertical velocity characteristics.

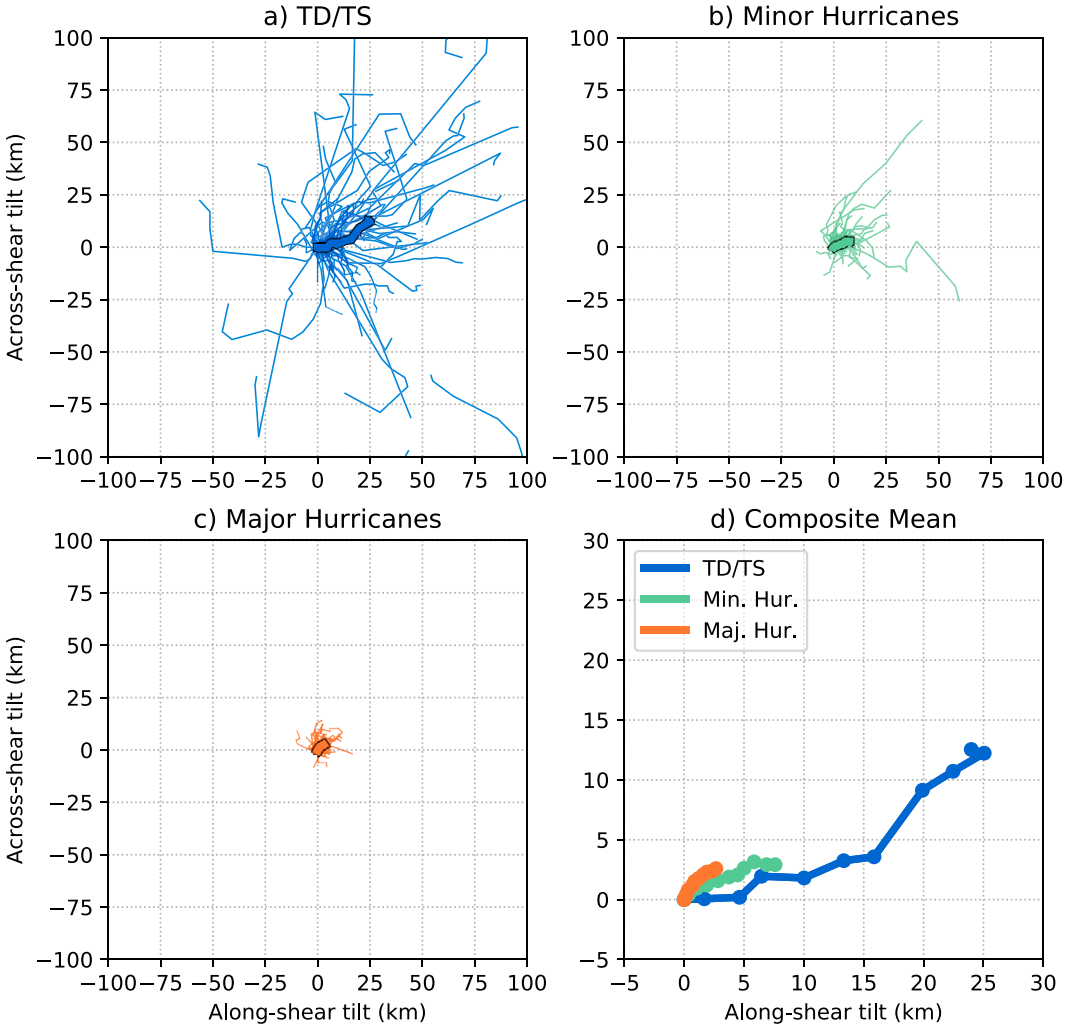

FIG. 10. (a) Shear-relative hodographs of vortex tilt (km) for TCs of tropical depression and tropical storm intensity. Here, tilt is shown for the 2–7-km layer. Each thin line represents a unique TDR merged analysis, while the composite-mean tilt hodograph is shown by the thicker line. The vertical wind shear is defined by the 850–200-hPa deep-layer shear, which is oriented with a heading toward the right side of the panel. (b),(c) As in (a), but for TCs of minor hurricane intensity, and major hurricane intensity, respectively. (d) As in (a)–(c), but zoomed in to display the composite-mean tilt profile for each TC intensity group.

Although there is limited data coverage, the composite radial wind from Fig. 11 shows TCs of tropical depression and tropical storm intensity are associated with the deepest inflow of the three intensity groups (Fig. 11a). Here, we describe inflow depth using the total inflow in the lower troposphere, which likely includes contributions from both surface friction and diabatic heating. Although it is unclear to what extent the observed lower-tropospheric inflow is receiving contributions from surface friction and heating-induced inflow, the relatively deep inflow in weaker storms is consistent with previous observational work (Zhang et al. 2011) and theoretical studies, which have linked TC boundary layer depth to inertial stability (e.g., Kepert 2001, 2012). As TC intensity increases, inflow depth becomes shallower and the magnitude of inflow increases (Figs. 11b,c). This relationship between inflow and TC intensity is consistent with composites from dropsonde observations (Zhang et al. 2011); however, the TDR-derived composite inflow magnitudes in the present study are significantly weaker than those measured by dropsondes. The weaker TDR-derived inflow magnitudes are likely due to difficulty resolving the peak inflow at locations away from the flight track, which are observed by relatively large pulse volumes. More specifically, in the present study, which uses gridded three-dimensional analyses, winds are analyzed at an altitude as low as 0.5 km, but the radar sampling and quality control procedure will impact the wind retrieval there. Doppler radar pulse volumes contaminated by scattering from the ocean surface must be removed. Therefore, at increasing horizontal distance from the swath center, the weighted-mean altitude of Doppler observations contributing to the analysis at

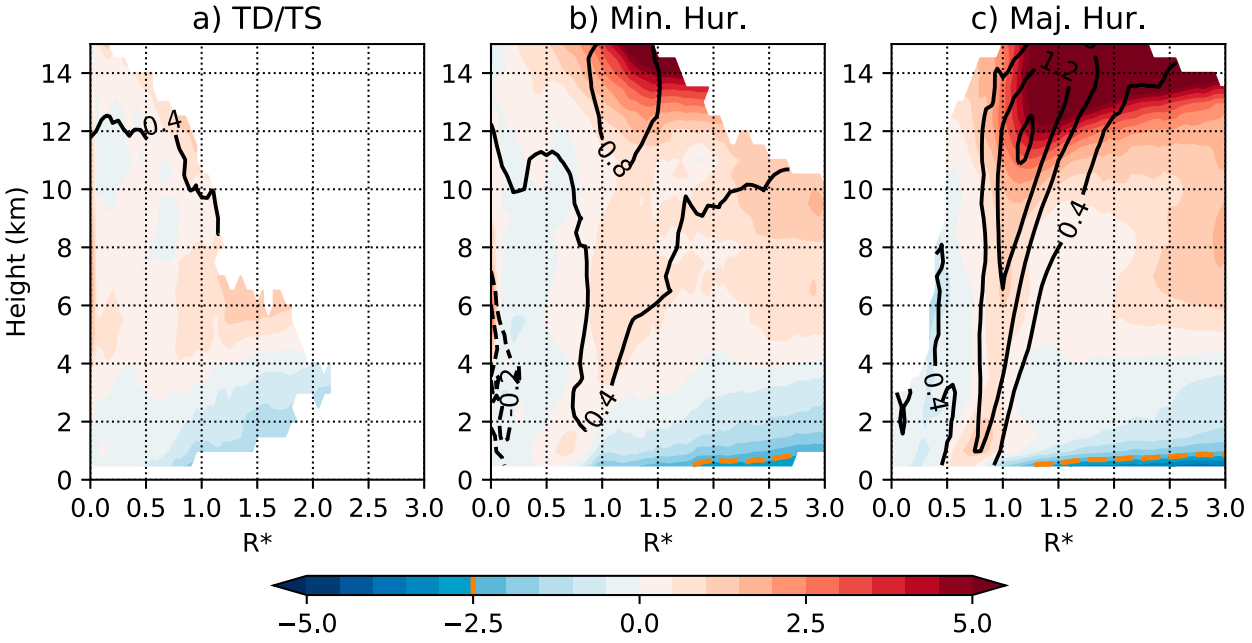

FIG. 11. (a) Composite-mean, azimuthally averaged radial wind ($\overline{V_R}$; shaded; m s^{-1}) and vertical velocity ($\overline{V_W}$; positive values contoured in solid, black lines every 0.4 m s^{-1}; negative values contoured in dashed, black lines every 0.2 m s^{-1}) for TCs of tropical depression and tropical storm intensity. The dashed, orange contour highlights differences in the extent of relatively strong inflow ($\overline{V_R} < 2.5$ m s^{-1}). Values are shown with respect to height (km) above sea level and normalized radius (R^*), where $R^* = 1$ is the radius of maximum wind at a height of 2 km. Composite values are only plotted for grid points where at least 20 merged analyses had observations. (b),(c) As in (a), but for TCs of minor hurricane and major hurricane intensity, respectively.

0.5 km will increasingly exceed 0.5 km to the point that no Doppler data fall within the vertical cutoff distance of the interpolation and the grid point is flagged. In addition, the variational method's use of a continuity constraint in the boundary layer where the vertical structure of divergence is not well resolved will also introduce some error into the retrieval there. Furthermore, the peak inflow in the TC boundary layer is typically found at heights below 0.5 km (e.g., Zhang et al. 2011) and, therefore, the inflow magnitudes seen in Fig. 11 are not representative of the peak inflow layer. These issues demonstrate that caution should be used when using these gridded TDR analyses to describe processes occurring in the TC boundary layer.

The uncertainty of the near-surface observations notwithstanding, Fig. 11 shows azimuthally averaged vertical velocity ($\overline{V_W}$) associated with the ascending branch of the TC secondary circulation increases with increasing TC intensity. In all intensity groups, maximum $\overline{V_W}$ values are found in the upper-troposphere between heights of 10–14 km, which agrees with previous radar-based observations of TCs (Heymsfield et al. 2010; Rogers et al. 2012). For TCs of hurricane intensity, the slope of the TC eyewall is apparent, as the corridor of largest $\overline{V_W}$ shifts to larger radii with height (Figs. 11b,c). Near the top of the eyewall updraft, the outflow layer can be seen; however, the outflow layer is not completely resolved in these composites due to the coverage constraints imposed. Despite some uncertainty in the radial flow structure of these composites, Fig. 11 suggests the TC secondary circulation becomes increasingly robust as TC intensity increases.

To better visualize the relationship between TC intensity and ascent in the inner core of the TC, Fig. 12 shows how the maximum $\overline{V_W}$ for each merged TDR analysis at a height of 8 km[3] varies as a function of TC intensity. Figure 12 shows that although some variability exists, a robust relationship is observed between TC intensity and maximum $\overline{V_W}$. There are signs of a nonlinear relationship between TC intensity and the maximum azimuthally averaged ascent, as suggested by the increasingly large maximum $\overline{V_W}$ for TCs $>$ 115 kt, although some uncertainty exists due to the relatively small sample size at these large intensities.

b. *Distribution of TC inner-core vertical velocities in different intensity regimes*

Thus far, we have demonstrated the azimuthally averaged TC secondary circulation is closely related to TC intensity. However, it is unclear whether more intense TCs are associated with larger $\overline{V_W}$ within the TC inner core because the maximum ascent is stronger in more intense TCs, or simply because ascent is more widespread in intense TCs, and therefore would have a stronger projection onto the azimuthal mean. We will now investigate how the distribution of vertical velocity in the TC inner core varies by TC intensity.

Figure 13 shows select percentiles of V_W for each TC intensity group using all observations within a 300 km $\times$ 300 km

[3] A height of 8 km yielded the most robust relationship between $\overline{V_W}$ and TC intensity from the multiple levels examined.

TABLE 3. Best track intensity (V_{max}) bounds and the number of TDR swath and merged analyses for the three TC intensity groups where sufficient data coverage was present to examine TC convective characteristics (using TCs between 2010 and 2020).

TC intensity group	Intensity range (kt)	No. of swath analyses	No. of merged analyses
TD/TS	$V_{max} < 64$	195	61
Minor hurricane	$64 \leq V_{max} < 96$	190	57
Major hurricane	$V_{max} \geq 96$	172	47

TC-centered box. Each intensity group is comprised of over a million observations of V_W at each height between 1 and 12 km, indicating a very robust sample size (Fig. 13a). Figure 13b shows little difference in V_W between the 10th and 90th percentiles for each intensity group. Some differences emerge, however, when focusing on the lower and upper tails of the distributions. For instance, for heights above 10 km, the 99.9th percentile of V_W for each intensity group is largest for TCs below hurricane intensity (Fig. 13b). Alternatively, in the lower troposphere, the 99th percentile of V_W for each group is largest for major hurricanes. In the lower tail of the distribution, major hurricanes have slightly stronger descent than weaker TCs between 4 and 12 km, as seen by the first percentile contour, whereas TCs below hurricane intensity have the strongest descent above 12 km.

The differences in the distribution of vertical velocities between TC intensity groups display a sensitivity to the radial region of the storm. Figure 14 shows a similar percentile analysis as Fig. 13, but here observations are constrained to either the TC eyewall region ($R^* = 0.75$–1.25) or the rainband region ($R^* = 1.5$–3.0). In the eyewall region (Fig. 14b), the differences in peak ascent between major hurricanes and weaker TCs is even more pronounced than when all data points are considered. Between heights of 4 and 8 km, the 99th percentile of V_W in major hurricanes exceeds the 99.9th percentile of V_W in both minor hurricanes and TCs below hurricane intensity. Major hurricanes are also associated with the strongest descent, as evidenced by the first percentile of V_W. Alternatively, in the TC rainband region, there are minimal differences in the distribution of V_W in the lower troposphere. Above 4 km, the distributions of V_W begin to diverge at the upper end of the V_W distribution, with relatively weak TCs displaying the largest peak ascent.

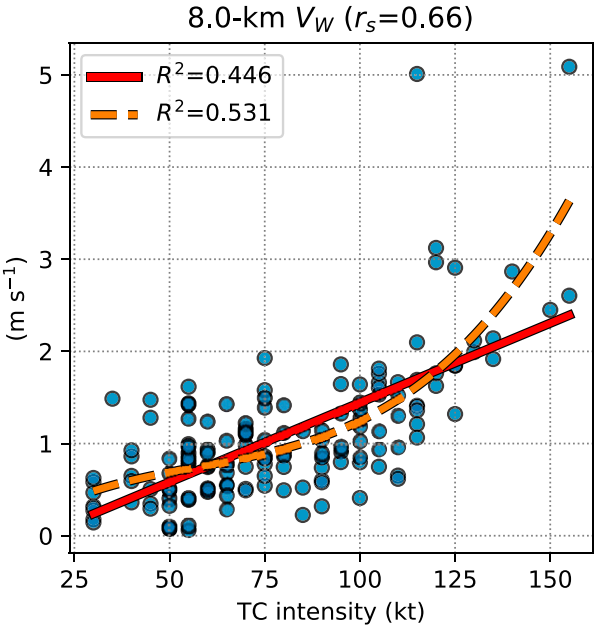

FIG. 12. Scatterplot of the maximum azimuthally averaged vertical velocity ($\overline{V_W}$; m s^{-1}) at a height of 8 km, as a function of best track TC intensity (kt). Each point represents a unique merged analysis. A linear fit to the distribution is shown by the red, solid line, and a cubic polynomial fit is shown by the dashed, orange line. The square of the correlation coefficients (R^2) is shown in the legend. The rank correlation coefficient is denoted by r_s.

This V_W analysis reveals that although TCs of major hurricane intensity have more robust azimuthally averaged overturning circulations than weaker TCs, storms below hurricane intensity have a greater frequency of the most extreme vertical velocities in the upper troposphere, especially outward of the inner core. Additionally, the percentile analysis suggests that the strongest ascent (i.e., the top 0.1% of V_W) in relatively weak TCs occurs within an environment of greater buoyancy than the regions of strongest ascent in major hurricanes, as the 99.9% contour of V_W in weak TCs displays a greater acceleration with height in both the eyewall and rainband region above 4 km, whereas the largest ascent in major hurricanes increases more gradually with height over this same layer (Fig. 13b). We therefore hypothesize that the convection in the major hurricanes sampled here occurs in an environment approaching moist symmetric neutrality (Emanuel 1986).

It is unclear why the strongest peak ascent in the lower-tropospheric eyewall region occurs in major hurricanes, but it is possible this ascent is forced by stronger convergence in the planetary boundary layer associated with stronger inflow into the TC eyewall (e.g., Zhang et al. 2011). It is also possible mesovortices at the eye–eyewall interface contribute to the larger lower-tropospheric peak ascent in major hurricanes (Marks et al. 2008; Stern et al. 2016); however, such features are likely too small to be properly resolved by the 2-km horizontal grid spacing of the TDR analyses used here. Other potential sources of uncertainty in this V_W analysis include the inability to separate buoyantly driven accelerations from dynamic accelerations in the vertical velocity field as well as the inability to sample the vertical structure of individual updrafts.

5. Discussion

The results presented here demonstrate strong relationships exist between TC intensity and TC vortex and convective

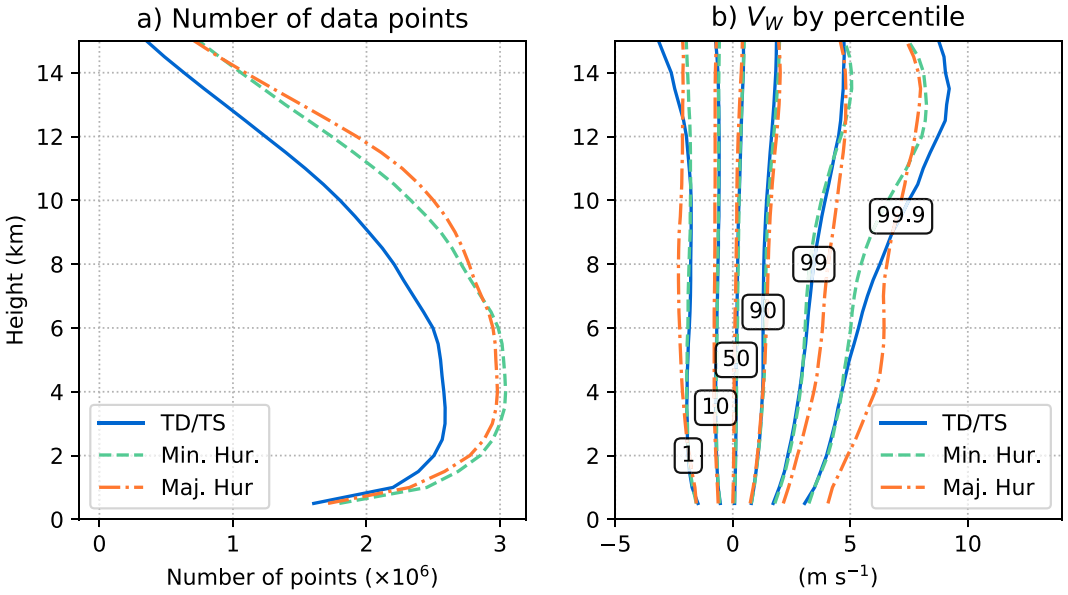

FIG. 13. (a) Number of V_W observations within a 300 km × 300 km TC-centered box for TCs of tropical depression and tropical storm intensity (solid; blue line), minor hurricane intensity (dashed; green line), and major hurricane intensity (dash–dotted, orange line) at each analysis height. Here, we solely consider TDR swath analyses. Note the observation counts are scaled by 10^6. (b) Vertical profiles of specified percentiles of V_W for each intensity group. The styles of the lines correspond to those shown in (a). The percentiles shown here are the 1%, 10%, 50%, 90%, 99%, and 99.9% of all V_W observations for the specified intensity group at a given height. For reference, the profiles are also labeled by the corresponding percentile.

characteristics. As TC intensity increases, we have found that the TC vortex structure becomes increasingly organized, with a significant reduction in the distribution of vortex tilt (Figs. 9 and 10) and a shift in the radial vorticity profile from a monopole to a ring-like maximum in the lower troposphere (Fig. 7). Additionally, the convective structure becomes better organized, as the azimuthally averaged overturning circulation becomes more robust (Figs. 11 and 12). Our results agree with satellite-derived observations that show an increase in TC convective organization with increasing TC intensity (Dvorak 1975; Velden et al. 2006; Fischer et al. 2018).

These findings suggest that as TC intensity increases, an increasingly organized vortex and convective structure are necessary to sustain a given TC intensity, such that a sufficiently strong overturning circulation imports enough angular momentum to balance the angular momentum sink of frictional torque in the TC boundary layer (Smith and Montgomery 2015). This notion is supported by idealized modeling studies, which have shown that TC intensity is strongly correlated with area-averaged, lower-tropospheric vertical mass flux (Alland et al. 2021). It appears plausible that steady-state TCs are associated with a base-state vortex and convective structure which supports the intensity of the storm. Thus, any deviations from the base-state TC vortex and convective structure for a given intensity (i.e., the anomalous TC structure) can lead to changes in TC intensity as the storm shifts toward a new equilibrium, which would be the intensity supported by the present TC structure. This hypothesis is supported by the results of Cecil and Zipser (1999), who showed area-averaged convective metrics observed from low-Earth orbiting satellites are more closely correlated to future TC intensity than the current intensity of the storm. Likewise, Fischer et al. (2018) showed that the anomalous convective signature identified by geostationary and low-Earth orbiting satellites is strongly related to TC intensity change. Although the present study has only shown how the TC kinematic structure is related to TC intensity, we have laid the framework for future studies to test the hypothesis that TC intensity change is closely related to the anomalous TC kinematic and convective structure.

Despite the strong signals found in this study, the radar analyses examined here contain some caveats, which should be acknowledged. Among them is the use of merged analyses to diagnose aspects of TC vortex structure. Because merged analyses are constructed from swaths of TDR observations typically collected over a 3–5-h sampling period, any changes in the vortex structure in regions of the TC that are repeatedly sampled are smoothed in the compositing process. For example, in a hypothetical, tilted TC, if the midlevel TC vortex is precessing about the low-level TC center during the flight, the merged TDR analysis of the vortex structure will not necessarily reflect the change in the direction and magnitude of tilt that occurred over the observing period (e.g., Ryglicki et al. 2021). Instead, the approximate mean tilt configuration over the course of the mission will be portrayed. Thus, these TDR analyses differ from frameworks such as numerical modeling simulations, where instantaneous snapshots of the TC vortex structure are available at high temporal resolution.

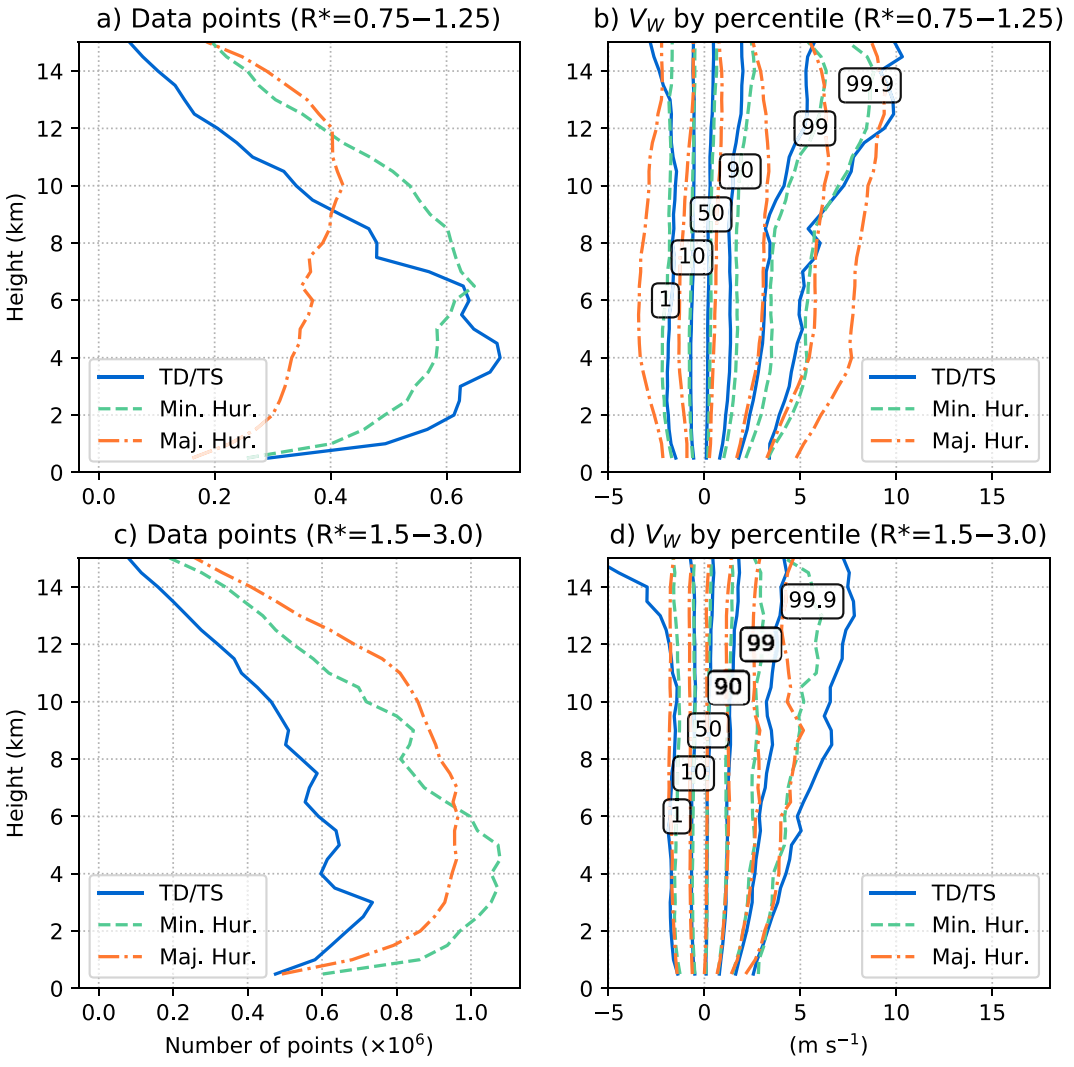

FIG. 14. As in Fig. 13, but only using observations within (a),(b) the eyewall region (R^* = 0.75–1.25) and (c),(d) the rainband region (R^* = 1.5–3.0).

The analyses of the TC vortex structure presented here are also limited to regions where sufficient scatterers exist to retrieve reliable radar observations. This limitation introduces a bias in the composite structures of azimuthally averaged fields, as well as the analyses of the vertical velocity distribution in the TC inner core, as regions devoid of hydrometeors cannot be sampled by the TDR. When accounting for the well-known precipitation asymmetries induced by vertical wind shear (Corbosiero and Molinari 2003; Reasor et al. 2013; DeHart et al. 2014), it is likely that to some extent, the results shown here are skewed toward observations in the downshear regions of the storm. Any potential sampling bias is likely to be more pronounced in weaker TCs, which have been shown to have more prominent convective asymmetries (Fischer et al. 2018; Ruan and Wu 2018).

6. Conclusions

We have performed a comprehensive observational analysis on how the three-dimensional kinematic TC inner-core structure is related to TC intensity. This was accomplished by using a novel airborne radar database, referred to as TCRADAR, which is comprised of over 900 radar analyses of inner-core TC structure for a wide range of TC intensities. The main findings of this study are listed below:

- As TC intensity increases, the radial gradient of the tangential wind field becomes sharper and the radial profile of vorticity transitions from a monopole toward a ring-like maximum located inward of the RMW.
- Relatively intense TCs are associated with a vertical profile of azimuthally averaged tangential wind that decays more

slowly with height and have significantly smaller vortex tilts than weaker TCs.
- TC intensity appears strongly connected to the vigor of the TC overturning circulation, as intense TCs display shallower and stronger lower-tropospheric inflow and stronger azimuthally averaged ascent than weaker storms.
- The distribution of vertical velocity varies with TC intensity, height, and radial region. In the lower troposphere, major hurricanes have the strongest peak ascent, especially within the eyewall region, whereas TCs below hurricane intensity have the widest range of vertical velocities in the upper troposphere, especially outward of the inner core.

This study also showcases the utility of TC-RADAR, which provides a homogeneous observational framework to examine TC inner-core kinematic characteristics. The database should continue to grow in the future as older analyses are reprocessed and new storms are observed as part of the annual hurricane field campaign (Rogers et al. 2006, 2013b; Zawislak et al. 2022). It is our hope that TC-RADAR will be used by the broader research community to further our understanding of TC inner-core processes.

Ongoing research is using TC-RADAR to investigate whether TCs that undergo RI are associated with unique convective and vortex characteristics compared to TCs that intensify at more gradual rates. A separate project is also using TC-RADAR to explore how TC vortex tilt is connected to TC precipitation characteristics and TC intensity change for TCs below hurricane intensity, which has been shown here to be the intensity regime that has the greatest variability in tilt.

Multiple avenues for other future work exist. With the relationship between TC intensity and structure now established, it is our intent to examine how anomalous TC vortex and convective characteristics, relative to TC intensity, are linked to TC intensity change, similar to the satellite-based work of Fischer et al. (2018). Future work will also examine how the thermodynamic characteristics of the TC inner core are related to the vertical velocity signals identified in the present study, such as why peak ascent in mature TCs is is more pronounced lower in the troposphere compared to TCs below hurricane intensity. Finally, we believe TC-RADAR can benefit numerical model validation efforts to ensure high-resolution TC guidance is producing realistic kinematic structures.

Acknowledgments. This manuscript was improved from conversations with Drs. Sim Aberson and Xiaomin Chen (NOAA/AOML/Hurricane Research Division). Drs. Andrew Hazelton, Frank Marks, and Jonathan Zawislak provided helpful comments on this work during an internal review process. We are grateful for the meticulous comments and suggestions from two anonymous reviewers during peer review. We would also like to thank Tyler Green (University of Oklahoma) for assistance with testing and refining the novel TC center-finding algorithm. Drs. Mark DeMaria and Stephanie Stevenson (NOAA/NWS/National Hurricane Center) kindly provided the SHIPS diagnostic files. This work was partially supported by Office of Naval Research Award N00014-20-1-2057.

Data availability statement. TC-RADAR comprises two netCDF files (one for swath TDR analyses and one for merged TDR analyses), which are available at https://www.aoml.noaa.gov/ftp/pub/hrd/data/radar/level3/. This analysis used TC-RADAR version v3i. The SHIPS developmental data are located at https://rammb.cira.colostate.edu/research/tropical_cyclones/ships/developmental_data.asp.

APPENDIX

A Novel Center-Finding Technique

a. Center-finding procedure

In an effort to create an objective center-finding method that could more reliably identify the center of both weak and intense TCs, a novel algorithm was developed. Here, the TC center was determined as the analysis grid point that yielded the greatest similarity between the observed storm-relative horizontal wind and an idealized, symmetric, cyclonic flow field. This was achieved through an iterative approach, where a series of grid points are considered as potential TC center locations. For each potential TC center location, the similarity between the observed flow and the idealized vortex was determined via the following:

$$\epsilon = \frac{1}{n}\sum_{i=1}^{n} |\delta_i \alpha_i|, \tag{A1}$$

where ϵ is the average weighted deviation (i.e., error) between the observed storm-relative horizontal wind and the idealized, cyclonic vortex for all grid points with available TDR observations, n is the number of grid points with available data, i is the index of a given grid point, δ is a weighting function for the error and α is the angle of the deviation between the observed storm-relative horizontal wind direction and the idealized, cyclonic vortex centered on the potential TC center location to be tested. Here, δ and α are defined as follows:

$$\delta = a\frac{G}{\text{avg}(G)} + b\frac{|V_H|}{|V_{\text{max}}|}, \tag{A2}$$

$$G = \max\left\{\exp\left[-\left(\frac{r^2}{2R^2}\right)\right], 0.001\right\}, \tag{A3}$$

$$\alpha = \theta_{\text{obs}} - \theta_{\text{ideal}}, \tag{A4}$$

where a and b are arbitrarily determined coefficients used to weight the errors; G is a Gaussian-weighted distance function with a minimum bound of 0.001, where r is the radius of the given grid point from the potential TC center; R is a scaling radius used for weighting; avg indicates the average of all points with observations; $|V_H|$ is the magnitude of the storm-relative, horizontal wind at the given grid point; $|V_{\text{max}}|$ is the maximum magnitude of the storm-relative, horizontal wind in the analysis domain at the height of interest; and θ_{obs} and θ_{ideal} are the mathematical angles, in radians, of

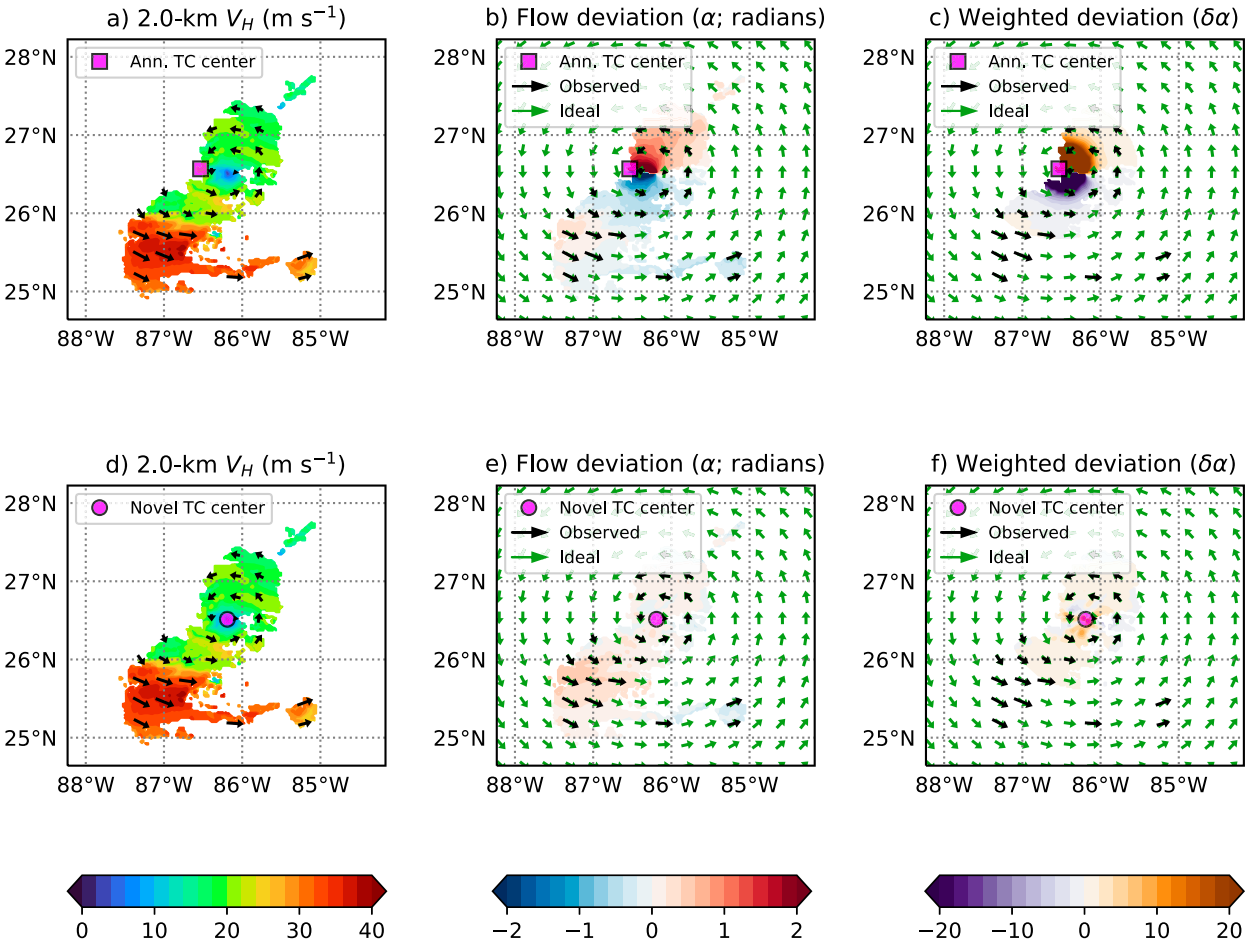

FIG. A1. (a) Storm-centered, motion-relative, TDR-derived horizontal wind speed (shaded; m s^{-1}) at a height of 2 km for a select center pass from the 120827H2 mission into Tropical Storm Isaac. The wind direction is shown by the black vectors. Observations are collected over a period spanning approximately 2100–2219 UTC 27 Aug 2012. The TC center estimate from the annulus-based tangential wind maximization technique is shown by the magenta square. (b) As in (a), but here an idealized, symmetric vortex (green vectors) has been centered on the annulus-based TC center estimate. The wind direction difference (α; radians) between the observed wind field in (a) and the idealized vortex is shaded. (c) As in (b), but for the weighted difference between the idealized cyclonic vortex and the observed flow ($\delta\alpha$). (d)–(f) As in (a)–(c), but for the optimal TC center estimate derived from the novel center-finding technique, shown by the magenta circle.

the observed flow field and the idealized, cyclonic vortex, respectively.

As can be seen from Eq. (A2), δ consists of two terms. The numerator of the first term, G, amplifies errors closer to the potential TC center. The first term in δ is normalized by the mean value of G to account for differences in observational coverage as the iterative center-finding algorithm searches the analysis domain. Without this normalization, a proposed grid point without observations near the TC center may yield relatively low values of δ due to the Gaussian weighting and, therefore, would be more likely to be determined the TC center location simply because of poor observational coverage. The second term in δ weights errors at each grid point proportionally to the ratio of the wind speed relative to the maximum observed wind speed in the analysis such that angle deviations at grid points with stronger wind are weighted more heavily. Through a series of sensitivity tests (not shown), we determined that setting the coefficients $a = 5$, $b = 2$, and $R = 25$ km more consistently yielded TC center estimates that agreed with subjectively determined TC centers based on centers of circulation and regions of enhanced vorticity.

Equations (A1)–(A4) consider all grid points with observations within 100 km from the potential TC center location. This radial constraint places a focus on the TC inner core and was particularly beneficial for identifying the TC center in weak TCs with asymmetric and broad outer circulations. Additionally, we require at least 15% of all grid points within 100 km of the TC center to contain observations. If the 15% coverage criterion is not satisfied, no center estimate is made for the swath. This coverage requirement was subjectively determined to provide a reasonable balance between ensuring enough observations were present to yield a confident center estimate while not rejecting a

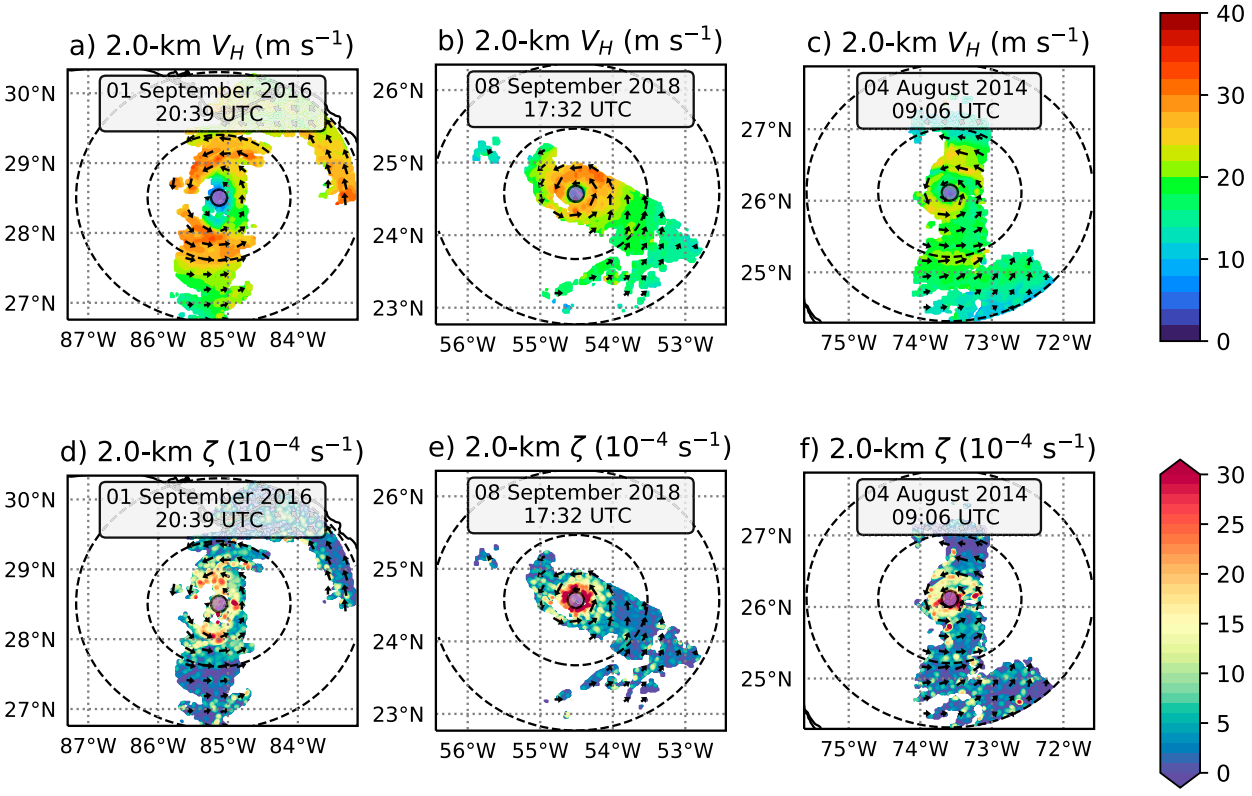

FIG. A2. (a) Storm-centered, motion-relative, TDR-derived horizontal wind speed (shaded; m s^{-1}) at a height of 2 km for a select center pass from the 160901I2 mission into Hurricane Hermine. The wind direction is shown by the black vectors. The approximate time of the analysis is displayed in the upper inset of the figure. The optimal re-centered TC location is shown by the purple circle. Black-dashed radial rings are shown in 100-km increments, which are displayed on a cylindrical equidistant map projection. (b) As in (a), but for the 180908H2 mission into Tropical Storm Florence. (c) As in (a), but for the 140804I1 mission into Tropical Storm Bertha. (d)–(f) As in (a)–(c), but for 2-km relative vorticity (shaded; 10^{-4} s^{-1}).

large number of TDR analyses for having insufficient coverage.

To save computational time, Eq. (A1) was computed iteratively using potential TC centers within a subset of the original analysis domain. During the first iteration, potential TC centers are selected incrementally, where only one out of every four grid points are considered in both the meridional and zonal directions within a 64 km × 64 km region, typically centered on the central grid point of the original TDR analysis domain. For the next step, using the grid point that yielded the lowest value of ϵ from the coarse grid, we tested all nearby grid points at the native 2-km horizontal grid spacing within a 16 km × 16 km domain as potential TC centers in the calculation of Eq. (A1). This step was repeated until the same potential TC center location yielded the lowest value of ϵ over consecutive iterations and that grid point was determined to be the final TC center. For each iteration, the selection of a potential TC center is not dependent upon whether a wind observation is present at the grid point. Thus, a TC center can be identified at a grid point without any wind observations provided the aforementioned coverage criterion is still satisfied.

To summarize, for a given TDR analysis, we compute a mean error field ϵ of the difference between the observed flow and an idealized, cyclonic vortex of purely tangential flow for a series of potential TC center locations. The grid point that yields the lowest value of ϵ is determined to be the actual TC center location. An advantage of the novel center-finding technique was the robustness of the algorithm to sparse data coverage. We found that the novel technique allowed for the re-centering of individual TDR swath analyses, which otherwise use an initial TC center estimate based solely on the in situ flight-level winds, which can yield uncertain TC center estimates if the aircraft does not transect the center of circulation. Although the re-centering of swath data does not affect the TDR wind analysis itself, the re-centering facilitates more reliable analyses of the evolution of vortex- and convective-scale structures between consecutive center passes in a given reconnaissance mission, as well as the construction of more accurate merged analyses.

The novel method is reminiscent of the center-finding method described by Willoughby and Chelmow (1982), which utilized in situ flight-level wind. Both the Willoughby

and Chelmow (1982) center-finding approach and the novel method discussed here assume a preexisting circulation and apply a cost function to determine the TC center location; however, the novel technique uses a different cost function and does not require information on the aircraft's closest point of approach to the TC center. Although both techniques essentially attempt to identify the point that maximizes the storm-relative circulation within a given domain, we have found the novel technique to be particularly well suited for the greater horizontal data coverage provided by the TDR, compared to solely using flight-level wind.

b. Examples of the novel TC center-finding algorithm

A comparison of the novel center-finding algorithm with the objective center-finding method used in previous TDR composite studies is performed using TDR swath analyses of Tropical Storm Isaac (2012; Fig. A1). In Figs. A1a–c, the TC center was objectively determined from a method that maximizes the azimuthally averaged tangential wind within annuli centered on the RMW, similar to Reasor and Eastin (2012) and Rogers et al. (2012). It should be noted that for the sake of this comparison, we are ignoring any coverage constraints that may have been employed by the previous studies. Fig. A1a shows the TDR-derived, motion-relative, horizontal wind field at a height of 2 km. To compare this method with the novel method introduced in Eq. (A1), an idealized, cyclonic vortex centered on the annulus-based, tangential-wind maximization center is shown by the green vectors in Fig. A1b. The flow angle deviation (α) between the observed flow and the idealized flow is shaded. Using the annulus-based technique, the estimated TC center is located along the western edge of the swath, as this location maximizes the tangential component of the asymmetric region of peak winds to the south of the TC center. This location is west-northwest of the center of circulation, with northeasterly flow observed immediately to the east of the proposed TC center, where the idealized, cyclonic vortex is associated with southerly flow, which yields large values of α in this region (Fig. A1b). The corresponding weighted errors ($\delta\alpha$) for the annulus-based TC center estimate are shown in Fig. A1c.

Alternatively, Figs. A1d–f show the optimal TC center estimate from the novel center-finding technique, as determined by the grid point that produced the lowest value of ϵ. Here, the TC center is located within a region of locally weak flow, coincident with the center of circulation of the motion-relative flow (Fig. A1d). The direction of the observed flow closely agrees with the idealized vortex, yielding relatively small values of α (Fig. A1e) and $\delta\alpha$ (Fig. A1f) throughout the domain.

Based on a subjective examination of the entire TCRADAR database, TC center estimates derived from the novel center-finding method were typically collocated with regions of enhanced cyclonic vorticity. Three examples are shown in Fig. A2 for TCs with varying degrees of inner-core size and symmetry. In the first example, Hurricane Hermine (2016) is associated with an elliptical eyewall and a secondary wind maximum approximately 100–150 km to the east of the TC center (Figs. A2a,d). Nonetheless, the novel algorithm objectively identified a TC center location near the center of circulation of the motion-relative flow and within a region of enhanced relative vorticity, despite large gaps in data coverage radially inward of the RMW. In the second example, a TC center was again identified near the center of circulation and a local maximum in vorticity in Tropical Storm Florence (2018), even though the storm exhibited a more compact inner-core structure and slightly weaker peak winds (Figs. A2b,e). In the final example, Tropical Storm Bertha (2014) was the weakest of the three TCs shown, with an asymmetric inner-core wind field, a secondary wind maximum approximately 100 km to the south of the TC center, and a confluent flow pattern on the southeast side of the TC (Fig. A2c). Nonetheless, the novel center-finding method identified a center location embedded within a region of enhanced cyclonic vorticity, demonstrating the robustness of the algorithm (Fig. A2f).

REFERENCES

Alland, J. J., B. H. Tang, K. L. Corbosiero, and G. H. Bryan, 2021: Combined effects of midlevel dry air and vertical wind shear on tropical cyclone development. Part I: Downdraft ventilation. *J. Atmos. Sci.*, **78**, 763–782, https://doi.org/10.1175/JAS-D-20-0054.1.

Alvey, G. R., J. Zawislak, and E. Zipser, 2015: Precipitation properties observed during tropical cyclone intensity change. *Mon. Wea. Rev.*, **143**, 4476–4492, https://doi.org/10.1175/MWR-D-15-0065.1.

——, E. Zipser, and J. Zawislak, 2020: How does Hurricane Edouard (2014) evolve toward symmetry before rapid intensification? A high-resolution ensemble study. *J. Atmos. Sci.*, **77**, 1329–1351, https://doi.org/10.1175/JAS-D-18-0355.1.

——, M. Fischer, P. Reasor, J. Zawislak, and R. Rogers, 2022: Observed processes underlying the favorable vortex repositioning early in the development of Hurricane Dorian (2019). *Mon. Wea. Rev.*, **150**, 193–213, https://doi.org/10.1175/MWR-D-21-0069.1.

Bhatia, K. T., and D. S. Nolan, 2013: Relating the skill of tropical cyclone intensity forecasts to the synoptic environment. *Wea. Forecasting*, **28**, 961–980, https://doi.org/10.1175/WAF-D-12-00110.1.

Boehm, A. M., and M. M. Bell, 2021: Retrieved thermodynamic structure of Hurricane Rita (2005) from airborne multi–Doppler radar data. *J. Atmos. Sci.*, **78**, 1583–1605, https://doi.org/10.1175/JAS-D-20-0195.1.

Cangialosi, J. P., E. Blake, M. DeMaria, A. Penny, A. Latto, E. Rappaport, and V. Tallapragada, 2020: Recent progress in tropical cyclone intensity forecasting at the National Hurricane Center. *Wea. Forecasting*, **35**, 1913–1922, https://doi.org/10.1175/WAF-D-20-0059.1.

Cecil, D. J., and E. J. Zipser, 1999: Relationships between tropical cyclone intensity and satellite-based indicators of inner core convection: 85-GHz ice-scattering signature and lightning. *Mon. Wea. Rev.*, **127**, 103–123, https://doi.org/10.1175/1520-0493(1999)127<0103:RBTCIA>2.0.CO;2.

Chen, S. S., J. A. Knaff, and F. D. Marks, 2006: Effects of vertical wind shear and storm motion on tropical cyclone rainfall asymmetries deduced from TRMM. *Mon. Wea. Rev.*, **134**, 3190–3208, https://doi.org/10.1175/MWR3245.1.

Chen, X., and G. H. Bryan, 2021: Role of advection of parameterized turbulence kinetic energy in idealized tropical cyclone simulations. *J. Atmos. Sci.*, **78**, 3593–3611, https://doi.org/10.1175/JAS-D-21-0088.1.

——, Y. Wang, J. Fang, and M. Xue, 2018a: A numerical study on rapid intensification of Typhoon Vicente (2012) in the South China Sea. Part II: Roles of inner-core processes. *J. Atmos. Sci.*, **75**, 235–255, https://doi.org/10.1175/JAS-D-17-0129.1.

——, M. Xue, and J. Fang, 2018b: Rapid intensification of Typhoon Mujigae (2015) under different sea surface temperatures: Structural changes leading to rapid intensification. *J. Atmos. Sci.*, **75**, 4313–4335, https://doi.org/10.1175/JAS-D-18-0017.1.

——, J. A. Zhang, and F. D. Marks, 2019: A thermodynamic pathway leading to rapid intensification of tropical cyclones in shear. *J. Geophys. Res.*, **46**, 9241–9251, https://doi.org/10.1029/2019GL083667.

——, M. Xue, B. Zhou, J. Fang, J. A. Zhang, and F. D. Marks, 2021: Effect of scale-aware planetary boundary layer schemes on tropical cyclone intensification and structural changes in the gray zone. *Mon. Wea. Rev.*, **149**, 2079–2095, https://doi.org/10.1175/MWR-D-20-0297.1.

Chong, M., and J. Testud, 1996: Three-dimensional air circulation in a squall line from airborne dual-beam Doppler radar data: A test of coplane methodology software. *J. Atmos. Oceanic Technol.*, **13**, 36–53, https://doi.org/10.1175/1520-0426(1996)013<0036:TDACIA>2.0.CO;2.

Corbosiero, K. L., and J. Molinari, 2003: The relationship between storm motion, vertical wind shear, and convective asymmetries in tropical cyclones. *J. Atmos. Sci.*, **60**, 366–376, https://doi.org/10.1175/1520-0469(2003)060<0366:TRBSMV>2.0.CO;2.

DeHart, J. C., R. A. Houze, and R. F. Rogers, 2014: Quadrant distribution of tropical cyclone inner-core kinematics in relation to environmental shear. *J. Atmos. Sci.*, **71**, 2713–2732, https://doi.org/10.1175/JAS-D-13-0298.1.

DeMaria, M., and J. Kaplan, 1994: A Statistical Hurricane Intensity Prediction Scheme (SHIPS) for the Atlantic basin. *Wea. Forecasting*, **9**, 209–220, https://doi.org/10.1175/1520-0434(1994)009<0209:ASHIPS>2.0.CO;2.

——, M. Mainelli, L. K. Shay, J. A. Knaff, and J. Kaplan, 2005: Further improvements to the Statistical Hurricane Intensity Prediction Scheme (SHIPS). *Wea. Forecasting*, **20**, 531–543, https://doi.org/10.1175/WAF862.1.

——, C. R. Sampson, J. A. Knaff, and K. D. Musgrave, 2014: Is tropical cyclone intensity guidance improving? *Bull. Amer. Meteor. Soc.*, **95**, 387–398, https://doi.org/10.1175/BAMS-D-12-00240.1.

Dvorak, V. F., 1975: Tropical cyclone intensity analysis and forecasting from satellite imagery. *Mon. Wea. Rev.*, **103**, 420–430, https://doi.org/10.1175/1520-0493(1975)103<0420:TCIAAF>2.0.CO;2.

Emanuel, K, 1986: An air–sea interaction theory for tropical cyclones. Part I: Steady-state maintenance. *J. Atmos. Sci.*, **43**, 585–605, https://doi.org/10.1175/1520-0469(1986)043<0585:AASITF>2.0.CO;2.

——, and F. Zhang, 2016: On the predictability and error sources of tropical cyclone intensity forecasts. *J. Atmos. Sci.*, **73**, 3739–3747, https://doi.org/10.1175/JAS-D-16-0100.1.

Fischer, M. S., B. H. Tang, K. L. Corbosiero, and C. M. Rozoff, 2018: Normalized convective characteristics of tropical cyclone rapid intensification events in the North Atlantic and eastern North Pacific. *Mon. Wea. Rev.*, **146**, 1133–1155, https://doi.org/10.1175/MWR-D-17-0239.1.

——, ——, and ——, 2019: A climatological analysis of tropical cyclone rapid intensification in environments of upper-tropospheric troughs. *Mon. Wea. Rev.*, **147**, 3693–3719, https://doi.org/10.1175/MWR-D-19-0013.1.

——, R. F. Rogers, and P. D. Reasor, 2020: The rapid intensification and eyewall replacement cycles of Hurricane Irma (2017). *Mon. Wea. Rev.*, **148**, 981–1004, https://doi.org/10.1175/MWR-D-19-0185.1.

Frank, W. M., 1982: Large-scale characteristics of tropical cyclones. *Mon. Wea. Rev.*, **110**, 572–586, https://doi.org/10.1175/1520-0493(1982)110<0572:LSCOTC>2.0.CO;2.

Franklin, J. L., M. L. Black, and K. Valde, 2003: GPS dropwindsonde wind profiles in hurricanes and their operational implications. *Wea. Forecasting*, **18**, 32–44, https://doi.org/10.1175/1520-0434(2003)018<0032:GDWPIH>2.0.CO;2.

Galarneau, T. J., and C. A. Davis, 2013: Diagnosing forecast errors in tropical cyclone motion. *Mon. Wea. Rev.*, **141**, 405–430, https://doi.org/10.1175/MWR-D-12-00071.1.

Gamache, J. F., 1997: Evaluation of a fully three-dimensional variational Doppler analysis technique. Preprints, *28th Conf. on Radar Meteorology*, Austin, TX, Amer. Meteor. Soc., 422–423.

——, 2005: Real-time dissemination of hurricane wind fields determined from airborne Doppler radar data. Tech. Rep., National Hurricane Center, 38 pp., http://www.nhc.noaa.gov/jht/2003-2005reports/DOPLRgamache_JHTfinalreport.pdf.

——, F. D. Marks, and F. Roux, 1995: Comparison of three airborne Doppler sampling techniques with airborne in situ wind observations in Hurricane Gustav (1990). *J. Atmos. Oceanic Technol.*, **12**, 171–181, https://doi.org/10.1175/1520-0426(1995)012<0171:COTADS>2.0.CO;2.

Gao, J., M. Xue, A. Shapiro, and K. K. Droegemeier, 1999: A variational method for the analysis of three-dimensional wind fields from two Doppler radars. *Mon. Wea. Rev.*, **127**, 2128–2142, https://doi.org/10.1175/1520-0493(1999)127<2128:AVMFTA>2.0.CO;2.

Guimond, S. R., G. M. Heymsfield, and F. J. Turk, 2010: Multiscale observations of Hurricane Dennis (2005): The effects of hot towers on rapid intensification. *J. Atmos. Sci.*, **67**, 633–654, https://doi.org/10.1175/2009JAS3119.1.

——, M. A. Bourassa, and P. D. Reasor, 2011: A latent heat retrieval and its effects on the intensity and structure change of Hurricane Guillermo (1997). Part I: The algorithm and observations. *J. Atmos. Sci.*, **68**, 1549–1567, https://doi.org/10.1175/2011JAS3700.1.

——, G. M. Heymsfield, P. D. Reasor, and A. C. Didlake, 2016: The rapid intensification of Hurricane Karl (2010): New remote sensing observations of convective bursts from the Global Hawk platform. *J. Atmos. Sci.*, **73**, 3617–3639, https://doi.org/10.1175/JAS-D-16-0026.1.

——, J. A. Zhang, J. W. Sapp, and S. J. Frasier, 2018: Coherent turbulence in the boundary layer of Hurricane Rita (2005) during an eyewall replacement cycle. *J. Atmos. Sci.*, **75**, 3071–3093, https://doi.org/10.1175/JAS-D-17-0347.1.

Hazelton, A. T., R. Rogers, and R. E. Hart, 2015: Shear-relative asymmetries in tropical cyclone eyewall slope. *Mon. Wea. Rev.*, **143**, 883–903, https://doi.org/10.1175/MWR-D-14-00122.1.

——, R. E. Hart, and R. F. Rogers, 2017: Analyzing simulated convective bursts in two Atlantic hurricanes. Part II: Intensity change due to bursts. *Mon. Wea. Rev.*, **145**, 3095–3117, https://doi.org/10.1175/MWR-D-16-0268.1.

——, L. Harris, and S.-J. Lin, 2018: Evaluation of tropical cyclone structure forecasts in a high-resolution version of the multi-scale GFDL fvGFS model. *Wea. Forecasting*, **33**, 419–442, https://doi.org/10.1175/WAF-D-17-0140.1.

Hendricks, E. A., M. S. Peng, B. Fu, and T. Li, 2010: Quantifying environmental control on tropical cyclone intensity change. *Mon. Wea. Rev.*, **138**, 3243–3271, https://doi.org/10.1175/2010MWR3185.1.

Heymsfield, G. M., L. Tian, A. J. Heymsfield, L. Li, and S. Guimond, 2010: Characteristics of deep tropical and subtropical convection from nadir-viewing high-altitude airborne Doppler radar. *J. Atmos. Sci.*, **67**, 285–308, https://doi.org/10.1175/2009JAS3132.1.

Jiang, H., C. Tao, and Y. Pei, 2019: Estimation of tropical cyclone intensity in the North Atlantic and northeastern Pacific basins using TRMM satellite passive microwave observations. *J. Appl. Meteor. Climatol.*, **58**, 185–197, https://doi.org/10.1175/JAMC-D-18-0094.1.

Jones, S. C., 1995: The evolution of vortices in vertical shear. I: Initially barotropic vortices. *Quart. J. Roy. Meteor. Soc.*, **121**, 821–851, https://doi.org/10.1002/qj.49712152406.

Jorgensen, D. P., and J. D. DuGranrut, 1991: A dual-beam technique for deriving wind fields from airborne Doppler radar. Preprints, *25th Radar Meteorology Conf.*, Paris, France, Amer. Meteor. Soc., 458–461.

——, T. Matejka, and J. D. DuGranrut, 1996: Multi-beam techniques for deriving wind fields from airborne Doppler radars. *Meteor. Atmos. Phys.*, **59**, 83–104, https://doi.org/10.1007/BF01032002.

Kaplan, J., and Coauthors, 2015: Evaluating environmental impacts on tropical cyclone rapid intensification predictability utilizing statistical models. *Wea. Forecasting*, **30**, 1374–1396, https://doi.org/10.1175/WAF-D-15-0032.1.

Kepert, J. D., 2001: The dynamics of boundary layer jets within the tropical cyclone core. Part I: Linear theory. *J. Atmos. Sci.*, **58**, 2469–2484, https://doi.org/10.1175/1520-0469(2001)058<2469:TDOBLJ>2.0.CO;2.

——, 2012: Choosing a boundary layer parameterization for tropical cyclone modeling. *Mon. Wea. Rev.*, **140**, 1427–1445, https://doi.org/10.1175/MWR-D-11-00217.1.

Klotzbach, P. J., S. G. Bowen, R. Pielke, and M. Bell, 2018: Continental U.S. hurricane landfall frequency and associated damage: Observations and future risks. *Bull. Amer. Meteor. Soc.*, **99**, 1359–1376, https://doi.org/10.1175/BAMS-D-17-0184.1.

——, M. M. Bell, S. G. Bowen, E. J. Gibney, K. R. Knapp, and C. J. Schreck, 2020: Surface pressure a more skillful predictor of normalized hurricane damage than maximum sustained wind. *Bull. Amer. Meteor. Soc.*, **101**, E830–E846, https://doi.org/10.1175/BAMS-D-19-0062.1.

Knaff, J. A., and R. M. Zehr, 2007: Reexamination of tropical cyclone wind–pressure relationships. *Wea. Forecasting*, **22**, 71–88, https://doi.org/10.1175/WAF965.1.

——, S. P. Longmore, R. T. DeMaria, and D. A. Molenar, 2015: Improved tropical-cyclone flight-level wind estimates using routine infrared satellite reconnaissance. *J. Appl. Meteor. Climatol.*, **54**, 463–478, https://doi.org/10.1175/JAMC-D-14-0112.1.

Kossin, J. P., 2015: Hurricane wind–pressure relationship and eyewall replacement cycles. *Wea. Forecasting*, **30**, 177–181, https://doi.org/10.1175/WAF-D-14-00121.1.

——, and W. H. Schubert, 2001: Mesovortices, polygonal flow patterns, and rapid pressure falls in hurricane-like vortices. *J. Atmos. Sci.*, **58**, 2196–2209, https://doi.org/10.1175/1520-0469(2001)058<2196:MPFPAR>2.0.CO;2.

Krishnamurti, T. N., S. Pattnaik, L. Stefanova, T. S. V. V. Kumar, B. P. Mackey, A. J. O'Shay, and R. J. Pasch, 2005: The hurricane intensity issue. *Mon. Wea. Rev.*, **133**, 1886–1912, https://doi.org/10.1175/MWR2954.1.

Lorsolo, S., J. A. Zhang, F. Marks, and J. Gamache, 2010: Estimation and mapping of hurricane turbulent energy using airborne Doppler measurements. *Mon. Wea. Rev.*, **138**, 3656–3670, https://doi.org/10.1175/2010MWR3183.1.

——, J. Gamache, and A. Aksoy, 2013: Evaluation of the Hurricane Research Division Doppler radar analysis software using synthetic data. *J. Atmos. Oceanic Technol.*, **30**, 1055–1071, https://doi.org/10.1175/JTECH-D-12-00161.1.

Mallen, K. J., M. T. Montgomery, and B. Wang, 2005: Reexamining the near-core radial structure of the tropical cyclone primary circulation: Implications for vortex resiliency. *J. Atmos. Sci.*, **62**, 408–425, https://doi.org/10.1175/JAS-3377.1.

Marks, F. D., R. A. Houze, and J. F. Gamache, 1992: Dual-aircraft investigation of the inner core of Hurricane Norbert. Part I: Kinematic structure. *J. Atmos. Sci.*, **49**, 919–942, https://doi.org/10.1175/1520-0469(1992)049<0919:DAIOTI>2.0.CO;2.

——, P. G. Black, M. T. Montgomery, and R. W. Burpee, 2008: Structure of the eye and eyewall of Hurricane Hugo (1989). *Mon. Wea. Rev.*, **136**, 1237–1259, https://doi.org/10.1175/2007MWR2073.1.

Martinez, J., M. M. Bell, J. L. Vigh, and R. F. Rogers, 2017: Examining tropical cyclone structure and intensification with the FLIGHT+ dataset from 1999 to 2012. *Mon. Wea. Rev.*, **145**, 4401–4421, https://doi.org/10.1175/MWR-D-17-0011.1.

McBride, J. L., 1981: Observational analysis of tropical cyclone formation. Part I: Basic description of datasets. *J. Atmos. Sci.*, **38**, 1117–1131, https://doi.org/10.1175/1520-0469(1981)038<1117:OAOTCF>2.0.CO;2.

Montgomery, M., and R. Smith, 2014: Paradigms for tropical cyclone intensification. *Aust. Meteor. Oceanogr. J.*, **64**, 37–66, https://doi.org/10.22499/2.6401.005.

Nguyen, L. T., J. Molinari, and D. Thomas, 2014: Evaluation of tropical cyclone center identification methods in numerical models. *Mon. Wea. Rev.*, **142**, 4326–4339, https://doi.org/10.1175/MWR-D-14-00044.1.

——, R. F. Rogers, and P. D. Reasor, 2017: Thermodynamic and kinematic influences on precipitation symmetry in sheared tropical cyclones: Bertha and Cristobal (2014). *Mon. Wea. Rev.*, **145**, 4423–4446, https://doi.org/10.1175/MWR-D-17-0073.1.

Pielke, R. A., and C. W. Landsea, 1998: Normalized hurricane damages in the United States: 1925–95. *Wea. Forecasting*, **13**, 621–631, https://doi.org/10.1175/1520-0434(1998)013<0621:NHDITU>2.0.CO;2.

Reasor, P. D., and M. D. Eastin, 2012: Rapidly intensifying Hurricane Guillermo (1997). Part II: Resilience in shear. *Mon. Wea. Rev.*, **140**, 425–444, https://doi.org/10.1175/MWR-D-11-00080.1.

——, and M. T. Montgomery, 2015: Evaluation of a heuristic model for tropical cyclone resilience. *J. Atmos. Sci.*, **72**, 1765–1782, https://doi.org/10.1175/JAS-D-14-0318.1.

——, ——, and L. D. Grasso, 2004: A new look at the problem of tropical cyclones in vertical shear flow: Vortex resiliency. *J. Atmos. Sci.*, **61**, 3–22, https://doi.org/10.1175/1520-0469(2004)061<0003:ANLATP>2.0.CO;2.

——, ——, and L. F. Bosart, 2005: Mesoscale observations of the genesis of Hurricane Dolly (1996). *J. Atmos. Sci.*, **62**, 3151–3171, https://doi.org/10.1175/JAS3540.1.

——, M. D. Eastin, and J. F. Gamache, 2009: Rapidly intensifying Hurricane Guillermo (1997). Part I: Low-wavenumber structure and evolution. *Mon. Wea. Rev.*, **137**, 603–631, https://doi.org/10.1175/2008MWR2487.1.

——, R. Rogers, and S. Lorsolo, 2013: Environmental flow impacts on tropical cyclone structure diagnosed from airborne Doppler radar composites. *Mon. Wea. Rev.*, **141**, 2949–2969, https://doi.org/10.1175/MWR-D-12-00334.1.

Rios-Berrios, R., 2020: Impacts of radiation and cold pools on the intensity and vortex tilt of weak tropical cyclones interacting with vertical wind shear. *J. Atmos. Sci.*, **77**, 669–689, https://doi.org/10.1175/JAS-D-19-0159.1.

——, and R. D. Torn, 2017: Climatological analysis of tropical cyclone intensity changes under moderate vertical wind shear. *Mon. Wea. Rev.*, **145**, 1717–1738, https://doi.org/10.1175/MWR-D-16-0350.1.

——, C. A. Davis, and R. D. Torn, 2018: A hypothesis for the intensification of tropical cyclones under moderate vertical wind shear. *J. Atmos. Sci.*, **75**, 4149–4173, https://doi.org/10.1175/JAS-D-18-0070.1.

Ritchie, E. A., G. Valliere-Kelley, M. F. Piñeros, and J. S. Tyo, 2012: Tropical cyclone intensity estimation in the North Atlantic basin using an improved deviation angle variance technique. *Wea. Forecasting*, **27**, 1264–1277, https://doi.org/10.1175/WAF-D-11-00156.1.

Rogers, R., and Coauthors, 2006: The Intensity Forecasting Experiment: A NOAA multiyear field program for improving tropical cyclone intensity forecasts. *Bull. Amer. Meteor. Soc.*, **87**, 1523–1538, https://doi.org/10.1175/BAMS-87-11-1523.

——, S. Lorsolo, P. Reasor, J. Gamache, and F. Marks, 2012: Multiscale analysis of tropical cyclone kinematic structure from airborne Doppler radar composites. *Mon. Wea. Rev.*, **140**, 77–99, https://doi.org/10.1175/MWR-D-10-05075.1.

——, P. Reasor, and S. Lorsolo, 2013a: Airborne Doppler observations of the inner-core structural differences between intensifying and steady-state tropical cyclones. *Mon. Wea. Rev.*, **141**, 2970–2991, https://doi.org/10.1175/MWR-D-12-00357.1.

——, and Coauthors, 2013b: NOAA's Hurricane Intensity Forecasting Experiment: A progress report. *Bull. Amer. Meteor. Soc.*, **94**, 859–882, https://doi.org/10.1175/BAMS-D-12-00089.1.

——, P. D. Reasor, and J. A. Zhang, 2015: Multiscale structure and evolution of Hurricane Earl (2010) during rapid intensification. *Mon. Wea. Rev.*, **143**, 536–562, https://doi.org/10.1175/MWR-D-14-00175.1.

——, J. A. Zhang, J. Zawislak, H. Jiang, G. R. Alvey, E. J. Zipser, and S. N. Stevenson, 2016: Observations of the structure and evolution of Hurricane Edouard (2014) during intensity change. Part II: Kinematic structure and the distribution of deep convection. *Mon. Wea. Rev.*, **144**, 3355–3376, https://doi.org/10.1175/MWR-D-16-0017.1.

——, P. D. Reasor, J. A. Zawislak, and L. T. Nguyen, 2020: Precipitation processes and vortex alignment during the intensification of a weak tropical cyclone in moderate vertical shear. *Mon. Wea. Rev.*, **148**, 1899–1929, https://doi.org/10.1175/MWR-D-19-0315.1.

Ruan, Z., and Q. Wu, 2018: Precipitation, convective clouds, and their connections with tropical cyclone intensity and intensity change. *Geophys. Res. Lett.*, **45**, 1098–1105, https://doi.org/10.1002/2017GL076611.

Ryglicki, D. R., and D. Hodyss, 2016: A deeper analysis of center-finding techniques for tropical cyclones in mesoscale models. Part I: Low-wavenumber analysis. *J. Appl. Meteor. Climatol.*, **55**, 531–559, https://doi.org/10.1175/JAMC-D-15-0125.1.

——, J. D. Doyle, Y. Jin, D. Hodyss, and J. H. Cossuth, 2018: The unexpected rapid intensification of tropical cyclones in moderate vertical wind shear. Part II: Vortex tilt. *Mon. Wea. Rev.*, **146**, 3801–3825, https://doi.org/10.1175/MWR-D-18-0021.1.

——, C. S. Velden, P. D. Reasor, D. Hodyss, and J. D. Doyle, 2021: Observations of atypical rapid intensification characteristics in Hurricane Dorian (2019). *Mon. Wea. Rev.*, **149**, 2131–2150, https://doi.org/10.1175/MWR-D-20-0413.1.

Schecter, D. A., and K. Menelaou, 2020: Development of a misaligned tropical cyclone. *J. Atmos. Sci.*, **77**, 79–111, https://doi.org/10.1175/JAS-D-19-0074.1.

Schubert, W. H., M. T. Montgomery, R. K. Taft, T. A. Guinn, S. R. Fulton, J. P. Kossin, and J. P. Edwards, 1999: Polygonal eyewalls, asymmetric eye contraction, and potential vorticity mixing in hurricanes. *J. Atmos. Sci.*, **56**, 1197–1223, https://doi.org/10.1175/1520-0469(1999)056<1197:PEAECA>2.0.CO;2.

Shapiro, L. J., and H. E. Willoughby, 1982: The response of balanced hurricanes to local sources of heat and momentum. *J. Atmos. Sci.*, **39**, 378–394, https://doi.org/10.1175/1520-0469(1982)039<0378:TROBHT>2.0.CO;2.

Sitkowski, M., J. P. Kossin, C. M. Rozoff, and J. A. Knaff, 2012: Hurricane eyewall replacement cycle thermodynamics and the relict inner eyewall circulation. *Mon. Wea. Rev.*, **140**, 4035–4045, https://doi.org/10.1175/MWR-D-11-00349.1.

Smith, R. K., and M. T. Montgomery, 2015: Toward clarity on understanding tropical cyclone intensification. *J. Atmos. Sci.*, **72**, 3020–3031, https://doi.org/10.1175/JAS-D-15-0017.1.

——, ——, and N. V. Sang, 2009: Tropical cyclone spin-up revisited. *Quart. J. Roy. Meteor. Soc.*, **135**, 1321–1335, https://doi.org/10.1002/qj.428.

Stern, D. P., and D. S. Nolan, 2011: On the vertical decay rate of the maximum tangential winds in tropical cyclones. *J. Atmos. Sci.*, **68**, 2073–2094, https://doi.org/10.1175/2011JAS3682.1.

——, and G. H. Bryan, 2018: Using simulated dropsondes to understand extreme updrafts and wind speeds in tropical cyclones. *Mon. Wea. Rev.*, **146**, 3901–3925, https://doi.org/10.1175/MWR-D-18-0041.1.

——, J. R. Brisbois, and D. S. Nolan, 2014: An expanded dataset of hurricane eyewall sizes and slopes. *J. Atmos. Sci.*, **71**, 2747–2762, https://doi.org/10.1175/JAS-D-13-0302.1.

——, G. H. Bryan, and S. D. Aberson, 2016: Extreme low-level updrafts and wind speeds measured by dropsondes in tropical cyclones. *Mon. Wea. Rev.*, **144**, 2177–2204, https://doi.org/10.1175/MWR-D-15-0313.1.

Stevenson, S. N., K. L. Corbosiero, and J. Molinari, 2014: The convective evolution and rapid intensification of Hurricane Earl (2010). *Mon. Wea. Rev.*, **142**, 4364–4380, https://doi.org/10.1175/MWR-D-14-00078.1.

Tang, B., and K. Emanuel, 2012: A ventilation index for tropical cyclones. *Bull. Amer. Meteor. Soc.*, **93**, 1901–1912, https://doi.org/10.1175/BAMS-D-11-00165.1.

Trabing, B. C., and M. M. Bell, 2020: Understanding error distributions of hurricane intensity forecasts during rapid intensity changes. *Wea. Forecasting*, **35**, 2219–2234, https://doi.org/10.1175/WAF-D-19-0253.1.

Velden, C., and Coauthors, 2006: The Dvorak tropical cyclone intensity estimation technique: A satellite-based method that

has endured for over 30 years. *Bull. Amer. Meteor. Soc.*, **87**, 1195–1210, https://doi.org/10.1175/BAMS-87-9-1195.

Velden, C. S., and L. M. Leslie, 1991: The basic relationship between tropical cyclone intensity and the depth of the environmental steering layer in the Australian region. *Wea. Forecasting*, **6**, 244–253, https://doi.org/10.1175/1520-0434(1991)006<0244:TBRBTC>2.0.CO;2.

Wadler, J. B., R. F. Rogers, and P. D. Reasor, 2018: The relationship between spatial variations in the structure of convective bursts and tropical cyclone intensification as determined by airborne Doppler radar. *Mon. Wea. Rev.*, **146**, 761–780, https://doi.org/10.1175/MWR-D-17-0213.1.

Wang, Y., and G. J. Holland, 1996: Tropical cyclone motion and evolution in vertical shear. *J. Atmos. Sci.*, **53**, 3313–3332, https://doi.org/10.1175/1520-0469(1996)053<3313:TCMAEI>2.0.CO;2.

Wilks, D., 2011: *Statistical Methods in the Atmospheric Sciences.* 3rd ed. International Geophysics Series, Vol. 100, Academic Press, 704 pp.

Willoughby, H. E., and M. B. Chelmow, 1982: Objective determination of hurricane tracks from aircraft observations. *Mon. Wea. Rev.*, **110**, 1298–1305, https://doi.org/10.1175/1520-0493(1982)110<1298:ODOHTF>2.0.CO;2.

Wimmers, A., C. Velden, and J. H. Cossuth, 2019: Using deep learning to estimate tropical cyclone intensity from satellite passive microwave imagery. *Mon. Wea. Rev.*, **147**, 2261–2282, https://doi.org/10.1175/MWR-D-18-0391.1.

Yang, S., V. Lao, R. Bankert, T. R. Whitcomb, and J. Cossuth, 2021: Improved climatology of tropical cyclone precipitation from satellite passive microwave measurements. *J. Climate*, **34**, 4521–4537, https://doi.org/10.1175/JCLI-D-20-0196.1.

Zagrodnik, J. P., and H. Jiang, 2014: Rainfall, convection, and latent heating distributions in rapidly intensifying tropical cyclones. *J. Atmos. Sci.*, **71**, 2789–2809, https://doi.org/10.1175/JAS-D-13-0314.1.

Zawislak, J., and Coauthors, 2022: Accomplishments of NOAA's airborne hurricane field program and a broader future approach to forecast improvement. *Bull. Amer. Meteor. Soc.*, **103**, E311–E338, https://doi.org/10.1175/BAMS-D-20-0174.1.

Zhang, F., and D. Tao, 2013: Effects of vertical wind shear on the predictability of tropical cyclones. *J. Atmos. Sci.*, **70**, 975–983, https://doi.org/10.1175/JAS-D-12-0133.1.

Zhang, J. A., R. F. Rogers, D. S. Nolan, and F. D. Marks, 2011: On the characteristic height scales of the hurricane boundary layer. *Mon. Wea. Rev.*, **139**, 2523–2535, https://doi.org/10.1175/MWR-D-10-05017.1.